THESIS

TWO-PHOTON ABSORPTION LASER INDUCED FLUORESCENCE (TALIF) OF NEUTRAL XENON IN A HALL EFFECT THRUSTER PLASMA

Submitted by

James Thaddeus (Tad) Wegner

Department of Mechanical Engineering

In partial fulfillment of the requirements

For the Degree of Master of Science

Colorado State University

Fort Collins, Colorado

Fall 2021

Master's Committee:

Advisor: Azer P. Yalin

John Williams
Dylan Yost

ABSTRACT

TWO-PHOTON ABSORPTION LASER INDUCED FLUORESCENCE (TALIF) OF NEUTRAL XENON IN A HALL EFFECT THRUSTER PLASMA

This work presents measurements of ground state neutral xenon in the plume of a 1.5 kW Hall Effect thruster (HET) using two-photon absorption laser induced fluorescence (TALIF). Neutral xenon particles in the thruster plasma play an important role in ionization processes, overall energy conversion, and life-limiting interactions with surrounding wall materials in the thruster. Therefore, a detailed understanding of the neutral particle dynamics within the plume is desired. The TALIF diagnostic technique allows for laser induced excitation of xenon from its ground state using commercially available laser systems at accessible ultraviolet wavelengths (~222 nm). The signal collected from fluorescence of the excited atoms can be used to determine the local neutral density. We present a demonstration of TALIF first in a barium oxide (BaO) hollow cathode plume at varying radial positions, then in an HET plume at varying axial positions using fiber coupled collection optics with a spatial resolution of 3.14 mm^2. The detection limit of the TALIF measurement system 2.1 cm downstream of the thruster face was estimated to be 8 x 10^{17} m^{-3} as determined by comparison to a known reference signal. The ability to analyze ionization and thermal characteristics using these results is also discussed.

TABLE OF CONTENTS

CHAPTER 1: INTRODUCTION

1.1 Background and Motivation

Chemical propulsion systems are limited by the large mass fraction dedicated to the propellant. For deep space applications, this leads to a requirement of high mass utilization efficiency and limits the payload mass. In the 1960's, the scientific community began seriously pursuing electric propulsion (EP) as an alternative means of space travel with high specific impulse and mass utilization efficiency [1]. EP systems are well suited for deep space missions and in-space maneuvers like satellite station keeping. The most vigorously researched and well-developed EP devices are Ion Thrusters and Hall Effect Thrusters (HETs), both falling under the subgroup of electrostatic thrusters. To further advance EP as a reliable method of propulsion, emphasis has been placed on improving the thrust, efficiency, and lifetime of EP devices [2]. Improving these thruster properties requires a greater understanding of the dynamics of neutral (xenon) particles in the plasma propellant owing to their important role in ionization processes, overall energy conversion, and life-limiting interactions with surrounding wall materials.

The aforementioned processes involving neutral atoms are significantly influenced by Charge Exchange Collisions (CEX). As will be further discussed, in CEX processes, high energy ions in the plume accelerated by the applied electric field may collide with low energy neutral particles and exchange charge (an electron) in the process, resulting in a high energy neutral particle and low energy ion in the plume [3]. When these slow-moving ions are located near the thruster channel walls or an ion grid, they can be accelerated through a potential drop (plasma sheath), for example between the plasma and the wall. These ions can reach sufficient energy through the sheath to collide with the wall (or other components) and eject materials from it, i.e.

to cause physical sputtering, a process that manifests as erosion over time [3]. The frequency at which CEX occurs depends on (neutral) particle density and thus increases with pressure. The pressure dependence is of particular importance in ground testing of high power (~10-100 kW class) HET's since the pumping capabilities of state-of-the-art vacuum systems limit achievable base pressures [4]. In some cases, the higher pressures in ground testing means the thruster operation does not accurately mimic space conditions (so called "facility effects") [5]–[7]. Accordingly, being able to measure the xenon neutral density in the chamber will be very revealing to understand the propellant reactions and possible facility effects.

The present thesis addresses this gap by developing a TALIF diagnostic system to measure neutral xenon density in a Hall Effect thruster plasma. Such a measurement capability could support simulation and modeling efforts to accurately characterize facility effects and link to in-space thruster performance. As electric propulsion devices continue to earn a significant role in space propulsion, the work in this thesis seeks to aid in advancing space-based missions for exploration and satellite operation.

1.2 Electric Propulsion Theory

1.2.1 Rocket Propulsion

To properly introduce the operation of electric propulsion systems, it is important to first consider the theory that motivates their development. Understanding propulsion begins with Newton's second law of motion and applying the classical relationship for momentum:

$$\vec{F} = \frac{d\vec{p}}{dt} = \frac{d(m\vec{v})}{dt} \tag{1.1}$$

$$\vec{F} = \dot{m}\vec{v} + m\dot{\vec{v}} \tag{1.2}$$

where $\vec{F}$ is the net force acting on the system, $\vec{p}$ is the total momentum of the system, m is the mass, t is time, and $\vec{v}$ is the velocity. Taking the system to be a simple rocket in a gravitational field, the terms in Eq. 1.2 can be relabeled and reordered to describe the rocket's acceleration [1]**:**

$$\dot{\vec{v}} = \frac{\dot{m}\overrightarrow{u_e}}{m} + \frac{\overrightarrow{F_g}}{m} \tag{1.3}$$

where $\vec{u}_e$ is the exhaust velocity relative to the rocket, and $\overrightarrow{F_g}$ is the force of gravity. Because the rocket is ejecting its own mass to exchange momentum and propel forward, the $\dot{m}\vec{u}_e$ term on the right side that describes this momentum exchange interaction is known as the thrust. Considering in-space applications, where the force of gravity is negligible, and treating the exhaust velocity as a constant, Eq. 1.3 can be integrated to determine the net change in velocity, $\Delta\vec{v}$, accrued after ejecting some amount of mass Δm:

$$\Delta\vec{v} = \overrightarrow{u_e} \ln\left(\frac{m_0}{m_0 - \Delta m}\right) \tag{1.4}$$

where m_0 is the initial mass of the system (including mass of the payload, power supplies, rocket structural components, etc.). To define the lifetime of a propulsion device, which is used to determine the length of its mission, the denominator of the natural logarithm in Eq. 1.4 would become the final mass of the system, m_f, corresponding to consuming all of the propellant. The velocity change, Δv, simply referred to as "delta-v", quantifies the velocity increment needed in order to perform a particular in-space maneuver. In general, multiple maneuvers are needed to complete a mission; in which case, the total delta-v of a mission is given by the sum of the delta-v's of all necessary maneuvers. For example, a mission from Earth orbit to Mars orbit and back would require a total delta-v of around 10,000 m/s [1].

Space missions typically require the delivery of some payload mass to a desired location. In order to do this efficiently, it is desirable to have the initial mass of the system as close to the

final mass as possible. This would mean operators are maximizing the fraction of useful material to arrive at their mission objective. By manipulating Eq. 1.4, the ratio of final to initial mass of the system is shown to be a negative exponential of the ratio of the velocity increment to the exhaust velocity:

$$\frac{m_f}{m_0} = e^{-\frac{\Delta v}{u_e}} \tag{1.5}$$

From Eq. 1.5, it is apparent that to deliver a significant fraction of the initial mass to the final velocity, an exhaust velocity comparable to (or ideally much larger than) the mission delta-v is needed. Typical chemical propulsion exhaust velocities are on the order of 10^3 m/s, making them inefficient for long lifetime missions like deep-space exploration or satellite station-keeping, which have delta-v's on the order of 10^4 m/s or greater [1]. Selected mission delta-v's for solar system exploration are shown in Table 1.

Table 1: Example Δv for various space missions [1].

Mission	Δv [m/s]
Escape from earth surface (impulsive)	1.1×10^4
Earth orbit to Mars orbit and return	1.4×10^4
Earth surface to Mars surface and return	3.4×10^4
Earth orbit to Venus orbit and return	1.6×10^4
Earth orbit to Mercury orbit and return	3.1×10^4
Earth orbit to Jupiter orbit and return	6.4×10^4
Earth orbit to Saturn orbit and return	1.1×10^5

Chemical propulsion operates by inducing a combustion reaction that rapidly heats the propellant which then expands and accelerates through a nozzle. An alternative method of particle acceleration, which is capable of higher exhaust velocities, is to produce electrically charged particles and apply an electromagnetic body force. This approach is the fundamental concept behind the use of electric propulsion. In the case of electrostatic propulsion, positively charged ions are generated in a plasma and accelerated away from the thruster by a static electric field.

However, because the propellant mass is so low, the total amount of thrust generated is only on the order of milli-Newtons [8]. Although such thrust levels are far too small to escape the Earth's atmosphere, where air resistance and gravity would exceed the applied thrust, they are very adequate in the vacuum of space to accelerate a body to high velocities. More detailed aspects of electric propulsion, including HETs, are further discussed below

1.2.2 Key Concepts of Plasma Physics

A plasma is typically defined as a quasi-neutral ionized gas that exhibits collective behavior [9]. When a gas is (positively) ionized it means a significant fraction of the neutral atoms have been stripped of an electron, leaving a collection of free electrons, positively charged ions, and neutral atoms in the fluid (together termed as plasma). Negative ions are possible in some plasma systems but can generally be neglected for EP applications. For an ionized gas to be quasi-neutral, it must be sufficiently large and sufficiently populated with charged particles of each species that the net charge is effectively zero. The term quasi-neutral is used because in any arbitrary region of the plasma at any point in time, there may be a net positive or negative charge (imbalance) due to the stochastic nature of the particles' motion. Collective behavior refers to the concept that the motion of the particles in the plasma is not strictly dependent on applied external forces, but also on the electromagnetic interactions between the particles *within* the plasma. For example, if an external electric field is applied across a plasma, instead of seeing the electrons and ions accelerated in opposite directions indefinitely, the induced internal electric field caused by charge separation would (eventually) neutralize the influence of the external field.

Collective behavior plays a central role in the interaction of plasma with solid boundaries, for example chamber walls, and is thus integral to studying facility effects. Similar to a neutral gas, the particles in a plasma diffuse to fill an open space. Because electrons are a factor of ~10^2 –

10^5 times lighter than ions, they have higher mobility and diffuse much faster. As electrons reach the walls of a chamber, they tend to generate a region of electric potential lower than that of the bulk plasma. The resulting potential gradient repels electrons and attracts ions, generating a net positively charged region to balance the excess negative charge at the walls. This region, which is critical for the plasma-material interactions, is called the plasma sheath [9]. In particular, the ions that accelerate towards the wall can erode the wall material by physical sputtering (see below).

1.2.3 Hall Effect Thruster

A Hall Effect Thruster is an EP device that falls under the category of electrostatic propulsion. An HET typically consists of an annular channel across which an electric field points axially along the center line direction and a magnetic field points radially inward (Figure 1 [10]).

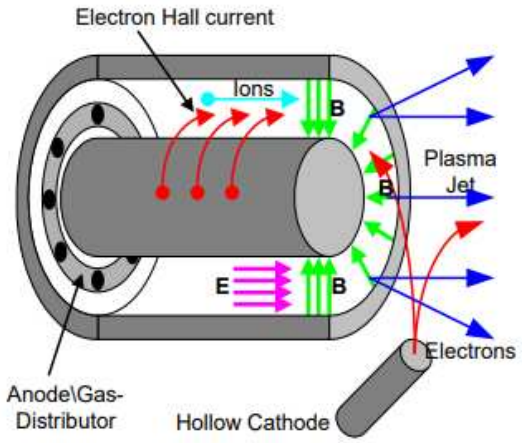

Figure 1: Hall effect thruster electric and magnetic field configuration.

The electric field is produced when the anode at the rear of the device is given a positive voltage (generally ~150-600V) relative to the exit plane [11]. The strong radial magnetic fields are produced by magnetic coils along the outer wall. The electric field serves the primary purpose of accelerating ions away from the device to generate thrust. However, these fields also attract

electrons toward the rear of the device (anode region). If unimpeded, these electrons would quickly transit to the anode where they would neutralize with little ionization occurring within the channel. However, the combined influences of the electric and magnetic fields tend to confine electrons to the channel, giving them opportunity to collide with neutral atoms and generate ions. More specifically, the electrons tend to circulate azimuthally (Hall current) due to the anomalous electron transport [1], the details of which are summarized below and which remain an area of active research. The weak magnetization of ions within the channel allows them to accelerate away relatively unimpeded (though hitting the channel walls in some cases).

A plasma is generated when primary electrons released from a hollow cathode ionize propellent atoms in the channel. The combined motion of gyration around the magnetic field lines and linear acceleration along the electric field lines results in an azimuthal drift velocity within the channel. This azimuthal drift of charged particles is referred to as a Hall Current, from which the device gets its name. The radius of a charged particle's gyration path around magnetic field lines (known as the Larmor radius) is given as:

$$r_L = \frac{m v_\perp}{|q| B} \tag{1.6}$$

where m is the mass of the particle, $v_\perp$ is the velocity component perpendicular to the field line, q is the electric charge, and B is the magnetic field strength. Electrons will tend to have small Larmor radii due to their low mass, meaning they are well confined to the channel by the magnetic field lines. Ions, on the other hand, are much more massive, so their radii can be larger than the channel width. The ions trajectory is then minimally affected by the magnetic field and can be accelerated axially away from the channel by the electric field. This electrostatic acceleration of ions is the mechanism by which the HET produces thrust.

In this description, with the electrons confined to the channel and the positively charged ions continually escaping, a net negative charge would develop within the HET. Eventually, if this charge were to continue to grow, the propellant ions in the plume would be accelerated back toward the thruster (or other elements of the device) reducing the thrust and potentially resulting in damage. To counter this charge buildup effect, (additional) electrons from an external hollow cathode recombine with the ions, thereby safely neutralizing them after they have already contributed to acceleration of the spacecraft.

1.2.4 Sputtering and Erosion

Ions present near the plasma sheath edge can be accelerated through the sheath (potential difference) between the HET plasma and channel wall. When the bombarding ions strike the wall, they deposit their kinetic energy into the wall material (lattice of atoms). If the deposited energy exceeds the binding energy of atoms within the surface (work function), then those atom(s) may leave the surface. This process of energetic ion bombardment can cause ejection of particles from the wall surface, a process referred to as physical sputtering [12]. Over long periods of time, the amount of sputtered (removed) material can increase ultimately causing the wall surface to erode away (or thin to a point that it becomes problematic). In HET applications, the lifetime of the thruster is in many cases limited primarily by the erosion of the boron nitride (BN) insulating channel [13], [14]. Eventually, degradation of this insulating surface generates an electrical short, preventing further plasma production and causing device failure. With background densities in ground-based facilities that can exceed in-space conditions, more sputtering events tend to occur, meaning facility tests can yield different lifetime estimates than would be observed during in-space operation. A quite recent advance in HET has been development of magnetic shielding (MS) approaches which, in short summary, reduce the sputter erosion (and increase channel lifetime) by

moving the ionization and acceleration regions further downstream of the channel [15]. While such thrusters have much less erosion, there is still a need to study facility effects and perform related studies, for example, to examine the operation and erosion away from standard operating points.

CEX reactions (themselves mediated by neutral density atoms) play a role in the sputter and erosion process. Recall that the electric field produces an acceleration out of the channel such that in many cases the ions leave the thruster channel without getting caught in the plasma sheath. However, if a CEX collision occurs, i.e., if a high energy ion (accelerated by the E-Field) and a low energy neutral (unaffected by electrostatic forces) collide (and an electron from the neutral atom is detached and transfers to the ion), then the result is a high energy neutral particle and low energy ion. In these cases, the low energy ion, lacking the dominant axial velocity vector component, can be more easily accelerated to the channel wall through the plasma sheath. This process can thus, over time, increase the rate of erosion. Because CEX requires the interaction of an ion with a neutral particle, the rate at which it occurs increases with the density of neutral particles in the region.

Testing of HETs on earth cannot match the low pressures of space (~ 10^{-13} Torr) [16], meaning there will always be a higher density of neutral particles present during testing than during a mission. One consequence of this is that the effect of CEX on the thruster walls will tend to be greater during tests, which must be accounted for when evaluating the lifetime of an HET over the course of a mission [5]. Recent studies have shown additional concerns regarding a net deposition of sputtered material on the magnetic pole pieces of a magnetically shielded plasma [17]. This deposition process can perturb the magnetic field topology, providing pathways for ions to accelerate to the insulator surface. Based on such considerations, accurate measurement of neutral

particles in an HET plasma are important to unraveling facility effects and to validate numeric models.

1.3 Measurement Theory

1.3.1 Alternative Diagnostics and Limitations

Measurement of neutral xenon density (n_{Xe}) poses a challenge for traditional plasma diagnostic methods. Physical probe diagnostic techniques typically consist of an insulated wire with an exposed tip placed directly in the plasma. In the case of a Langmuir probe, a voltage (differing from the plasma potential) is placed on the wire, causing ions and electrons in the surrounding plasma to be attracted or repelled from the wire (depending on the sign of the voltage difference) thereby generating a current which is recorded [18]. The variation of current against applied voltage provides the necessary information to extract the electron density and temperature in the plasma. Alternatively, for probing neutral particles, a thermocouple can be coated with particular metals that the neutral particles are highly reactive with [19]. This approach has been shown as especially useful with highly electronegative radicals. Reactions between the particles and metal coating generate heat near the thermocouple tip such that temperature readings can be used to extract particle densities [19]. Neutral xenon particles do not interact via the Coulomb interaction as ions do, nor do they readily recombine as radicals and reactive gases do. The absence of these interaction mechanisms acts as the primary limitation to most physical probe diagnostic methods.

A non-optical approach to neutral density measurement is provided by ionizing mass spectrometry. Ionization based diagnostics take advantage of the low ionization energy (~12 eV [20]) of xenon. The objective being to provide sufficient energy to ionize xenon gas atoms, typically by placing them in a potential field that exceeds their breakdown voltage. This is done

using two oppositely biased electrodes. In the case of a residual gas analyzer, the ions are introduced in an oscillating quadrupole potential field produced by four charged rods [21]. The ion moves within the potential field until its momentum allows it to reach and interact with one of the rods. The time it takes for this interaction to occur is dependent on the charge-to-mass ratio of the ion. Singly charged ions are related back to the atomic mass of xenon, indicating the presence of neutral xenon atoms. However, ionization diagnostics face several challenges in a plasma given the presence of charged species (ions) in the background plasma. The background of ions throughout the measurement volume needs to be accounted for to distinguish ions produced by the measurement device. The achievable spatial and temporal resolution of mass-spectrometry approaches should also be considered. Additionally, as with all physical probe diagnostics, the presence of the probe in the plasma produces a plasma sheath near its surface, perturbing the dynamics of the plasma particles and introducing complexity (often error) into each measurement. For this reason, in addition to those discussed above, optical diagnostics are a favored approach to neutral density measurement.

1.3.2 Laser Induced Fluorescence

Laser Induced Fluorescence (LIF) is a widely used laser diagnostic that has been applied to many fields including plasma diagnostics, combustion, and atmospheric science [22]. In the LIF technique, a collection of atoms (or molecules) absorbs incident laser light causing them to be promoted to a higher energy level [23] that then undergoes spontaneous emission down to the original state (in a resonant process) or some other lower state (in a non-resonant process). The light from this emission, known as fluorescence, is collected with a photodetector, typically a photomultiplier tube (PMT) for point measurements or an intensified camera for planar measurements, to give information on the species being probed. LIF is generally performed in one

of two regimes, weak-field or saturated depending on the intensity of the probe laser beam [22]. In the weak-field or linear regime (with weak laser excitation), the rate of de-population outweighs the pump rate and the excited state population remains well below the lower (initial) state population. In this regime, the fluorescence signal scales linearly with beam intensity and particle density (Figure 2 [24]). On the other hand, for higher laser power one enters a saturation regime where stimulated processes dominate and the excited state population becomes equal to that of the initial lower state (neglecting degeneracy). In this regime, the spontaneous emission (fluorescence signal) becomes independent of lower power (and is also unaffected by quenching). By removing the laser intensity dependence from the fluorescence signal, any noise due to laser power fluctuations is also removed (as are effects of quenching). A challenge, though, is to obtain

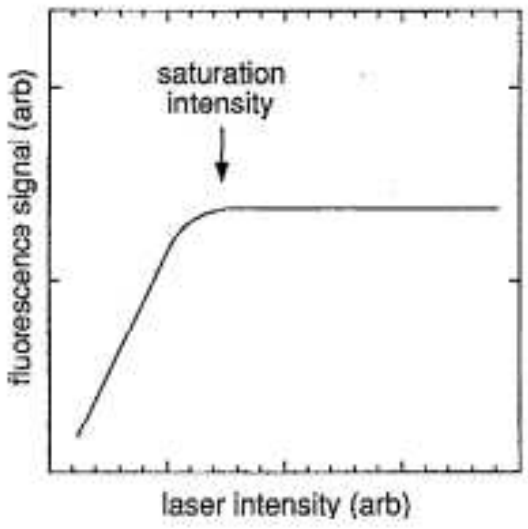

Figure 2: Fluorescence signal showing the transition from weak-field to saturation regime

saturation at the spatial and temporal edges of the pulse where the intensity inevitably decreases [22].

In regards to EP and measurements of the widely used xenon propellant, LIF has been used to measure excited state neutral xenon properties, with particular emphasis on determining velocity distributions [11], [25], [26]. These experiments have probed excited states (as the lower state of the LIF) owing to greater ease of accessing these states with available visible and near-infrared lasers. However, in order to reliably measure the overall population of target atoms (or molecules) from state-resolved laser measurements, one should measure the ground state, where a high fraction of the population resides given their Boltzmann population fractions. In the case of (neutral) xenon, the needed transitions from the atom's ground state to excited states have energy gaps far in the ultraviolet (~110-125 nm) precluding the use of available laser systems. A means to evaluate ground state neutral xenon densities is provided by Two-Photon Absorption Laser Induced Fluorescence (TALIF) as discussed below.

1.3.3 Two-Photon Absorption and TALIF

TALIF is a variant of LIF where the first absorption step, to promote the atoms to an excited state (from which they fluoresce) is based on two-photon absorption (versus typical single-photon). Two-photon absorption is a non-linear optical process first theorized by Goeppert-Mayer in 1931 [27]. Two-photons are simultaneously absorbed by an electron, exciting it to an upper state that is above the lower state by an energy gap equal to the sum of the energies of the two photons. TPA is dependent on the square of incident light intensity, so it tends to dominate over linear processes only at high intensity. For this reason, it was not observed experimentally until 1961, soon after the invention of the laser [28]. TPA can be described by perturbation theory. The electron's interaction with a single photon's electric field perturbs the energy spectrum in a manner that allows the second photon to be absorbed [29]. The electron, which occupied a stationary state of the atom, enters a superposition of energy states of the new atom-photon system. In this

superposition of states, often referred to as a virtual state, the electron can accept an additional photon to complete the absorption transition to the atom's excited energy state. Due to the time-energy uncertainty principle, the staying time of the electron in this superposition of states approaches zero [30]. This means the absorption of the second photon occurs effectively instantaneously with the first. The actual time between transitions is not precisely known, but must necessarily be shorter than the inverse of the bandwidth of the absorption line [31]. The incredibly short lifetime of the virtual state further explains why high light intensities are necessary, as two photons must interact with the same electron on very short time scales.

1.3.4 Xenon Spectroscopy and TALIF Scheme

The primary challenge facing laser induced fluorescence of xenon, and subsequently the reason for a TALIF approach to xenon density measurements, is that relatively high energy photons (~10 eV) are required to excite a ground state electron in a neutral xenon atom. The same mechanisms that determine electron excitation energy, primarily high valence shell stability (stronger bond) and high atomic number (weaker bond), determine the ionization energy of xenon (~12 eV). Though 10 eV is difficult to achieve through radiative processes like photon absorption, the slightly higher ionization threshold is readily accessible using collisional processes in plasma generation. Xenon is partly chosen as a propellant gas because of the ease with which it can be ionized, however, the comparable excitation barrier poses a major challenge for optical diagnostics.

TALIF does not require that the two photons carry the same energy, as long as the sum of their energies equals the energy spacing between the upper and lower states of the transition. However, resonant transitions, those in which the two photons are of equal energy, require only a single laser to interact with the gas. A set of resonant TALIF transitions from the Xe ground state

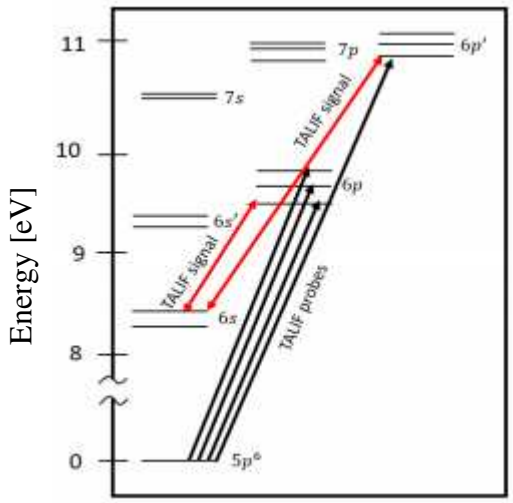

Figure 3: TALIF transition diagram.

and their relevant spectroscopic quantities are summarized in Table 2. Figure 3 provides a visual representation of the xenon energy levels and corresponding transition wavelengths, for the transitions described in Table 2. For example, to access the 6p upper state (from the ground state) requires a pair of photons with wavelength ~250 nm. Small changes between the energies of the 6p states are caused by differences in electron angular momentum. The 6p' states correspond to TALIF transitions near 220 nm. Both sets of upper levels decay to the same 6s metastable state in these examples.

Table 2: TALIF Transition Spectroscopic Quantities (ordered by excitation wavelength)

Excitation (Absorption step)			Fluorescence (Emission step)			
Wavelength [nm]	Upper State	Cross Section [10^{-35} cm^{-4}]	Wavelength [nm]	Lower State	Branching Ratio	Ref
222.5	$[^2P_{1/2}]6p'[1/2]_0$	55	788.7	$[^2P^o_{3/2}]6s'[1/2]^o_1$	0.62	[32]
224.2	$[^2P_{1/2}]6p'[3/2]_2$	50	834.7	$[^2P_{1/2}]6s'[1/2]^o_1$	0.73	[32]
			473.4	$[^2P^o_{3/2}]6s[3/2]^o_1$	0.027	[33]
225.1	$[^2P^0_{3/2}]7p[1/2]_0$		480.7	$[^2P^o_{3/2}]6s[3/2]^o_1$	0.25	[33]
			857.6	$[^2P^o_{1/2}]6s'[1/2]^o_1$	0.28	[33]
225.4	$[^2P^0_{3/2}]7p[3/2]_2$	0.68	462.4	$[^2P^o_{3/2}]6s[3/2]^o_2$	0.373	[33]
			484.4	$[^2P^o_{3/2}]6s[3/2]^o_1$	0.092	[33]
226.4	$[^2P^0_{3/2}]7p[5/2]_2$		469.7	$[^2P^o_{3/2}]6s[3/2]^o_2$	0.05	[34]
				$[^2P^o_{3/2}]6s[3/2]^o_2$	0.066	[33]
249.5	$[^2P_{3/2}]6p[1/2]_0$	7	828	$[^2P^o_{3/2}]6s[3/2]^o_1$	0.998	[35]
252.5	$[^2P_{1/2}]6p[3/2]_2$	2.4	823.2	$[^2P^o_{3/2}]6s[3/2]^o_2$	0.7	[35]
			894	$[^2P^o_{3/2}]6s[3/2]^o_1$	0.3	[33]
256	$[^2P_{1/2}]6p[5/2]_2$	4	904	$[^2P^o_{3/2}]6s[3/2]^o_2$	0.363	[35]
			992	$[^2P^o_{3/2}]6s[3/2]^o_1$	0.637	[33]

An interaction cross-section is a measure of the probability that a particular interaction will occur. The cross-section describes the probability based on the target particle having an effective interaction area. Should the incident particle pass within this effective area, the interaction will occur. Typical (single-photon) absorption cross-sections have units of cm^2. In TALIF, given that two photons are interacting with a target, the cross-section has units of cm^4.

The branching ratio is the number of times a specific electron decay transition occurs relative to the total amount of transitions from a given upper state (i.e., the probability that when a single upper state emits, it does so via the given transition). So, in the 222.5 nm excitation case, the excited electron will fluoresce with wavelength of 788.7 nm 62% of the time. In order to

maximize the TALIF signal, a high interaction cross-section and high branching ratio are desired. Further details of the relevant spectroscopic constants and associated equations are provided along with the TALIF population and signal-level modeling in Chapter 2.

1.3.5 Overview of Past Experiments on Xenon LIF and TALIF

LIF diagnostics have been applied to xenon as a means to study the physics and parameters of EP devices including HETs [11], [26], [36], [37]. Conventional (single-photon) Xe LIF has generally targeted velocity distribution profiles with laser wavelengths in the visible or near-infrared. Typically, a resonant scheme that excites and emits at 823 nm is used, with another scheme being excitation with 835 nm and non-resonant detection at 473.5 nm [11], [37]. Huang and Gallimore performed velocimetry measurements, reporting excited state neutral xenon velocities ranging from 100 m/s at the inlet to 300-400 m/s at the thruster exit plane [11]. Mazouffre outlines how LIF can be used to determine the electric field profile in a thruster plasma based on the ion velocity distribution [36]. A thorough description of the electric field profile provides insight into the spatial variation in collisional interactions between the neutral particles and the ions under the influence of the electric field.

For neutral density measurements (from the ground sate), TALIF has been researched over the last four decades [38], with early efforts dedicated to determination of spectroscopic quantities and evaluation of the gain and loss mechanisms for TALIF excited states [35], [38], [39]. In 1996, Crofton probed the 225.4 nm TALIF line (up to the $[^2P^0_{3/2}]7p[3/2]_2$ excitation state) in the T5 ion thruster plume to measure the axial xenon density profile, reporting a non-linear decay in density on the order of 10^{17} m^{-3} [40]. In 2007, Eichhorn et al. evaluated the performance in a cold gas cell of the 224.2 nm and 226.4 nm excitation schemes in addition to the 225.4 nm line that had been commonly used prior [34]. They concluded the three lines were similar in strength (i.e., within

30% of one another) and could all be potential TALIF options in EP studies. Kinefuchi et al. performed a similar study in a cold xenon gas, evaluating the 249.5 nm and 252.5 nm lines and measuring spontaneous decay rates of 3.7 x 10^7 s^{-1} for both lines [41]. Most comparable to the efforts of this thesis, in 2013 Crofton et al. used the 222.5 nm TALIF line to perform a detailed measurement of the radial and axial neutral density distribution in the plume of the SP-140 4.5 kW Hall thruster [42]. Similar to the 1996 paper, they report densities on the order of 10^{17} m^{-3} and a non-linear axial decay. They additionally elucidate a general behavior of the density reaching local maxima near the edges of the channel walls and minima inside the channel and through the thruster centerline. The present thesis seeks to build on these efforts by evaluating the detection limit of a TALIF system in these plasmas and decreasing the measurement spatial resolution to enable more detailed density profiles. The conclusion of the thesis revisits these past results in comparisons with those developed here.

1.4 Thesis Objectives and Outline

The overarching goal of the present thesis is to develop a TALIF measurement system for ground-state neutral xenon suitable for HETs to support related efforts on lifetime testing, facility effects and modeling. More specifically, we seek to develop a TALIF diagnostic with the following properties:

- Detection limit as low as 5 x 10^{15} m^{-3} in HET environment
- Spatial resolution as low as 5 mm
- Demonstrated on 1.5 kW HET

The sensitivity of the system - often a limiting factor - is determined primarily by its detection limit, with additional considerations including spatial resolution and ease of adaptability to

different HET test environments. A needed experimental step is to determine the best choice of absorption line (excitation wavelength) to maximize signal-to-noise ratio in the presence of plasma luminosity. This selection requires evaluation of both fluorescence collection from that line as well as analysis of the xenon plasma emission spectrum at or near that line. Additional tasks include performing measurements at minimum spatial resolution, in order to accurately map the density distribution, and developing the system such that measurements can be performed with relative ease and efficiency. Doing so assures accurate, repeatable measurements with the potential for comparison across devices.

The layout of the remainder of the thesis is as follows. Chapter 2 presents a basic numeric model of TALIF signals applicable to this research. Chapter 3 is dedicated to buffer gas (no plasma) measurements for initial selection of a TALIF line and system design (data acquisition system, optical train etc.). A buffer gas in a static pressure chamber with known xenon concentration is used to perform these measurements. The strength of the signal is the primary focus, with detector noise playing a secondary role. Chapter 4 builds on the work of Chapter 3 by incorporating xenon plasma background emission and the corresponding signal noise. These measurements are performed in the plume of a hollow cathode. Radial measurements are recorded to see how well the system captures spatial variations in neutral density. Chapter 5 tests the fully designed system in an HET plume, performing axial measurements to examine the spatial signal variation and detection limit. The concluding chapter summarizes the results of this work and makes suggestions for future work.

CHAPTER 2: RATE EQUATION MODEL FOR XENON TALIF

2.1 Model Formulation

A rate equation model for TALIF in a xenon gas has been developed to guide experimental design and interpret results. The model is presented here, starting in a general way, and then applied to neutral xenon atoms. In the weak-field regime, where our experiments are assumed to occur (see validating discussion in Section 4.4), a simple rate equation can be used to model the TALIF interaction. If the TPA process is strongly saturated, a complete density-matrix analysis would be required [38]. It is assumed that the ground state population is approximately constant (i.e., that we operate well below saturation), and that the pressure is low enough that quenching can be neglected for the chosen emission line. Later work in section 5.3.3 shows that quenching cannot be neglected using the 788.7 nm emission line. The rate equation for the excited state (upper level) population is given by [38]:

$$\frac{dN_2}{dt} = W_{12}^{2\nu} N_1^0 - \left(W_{23}^{i} + W_{21}^{2\nu} + T_2\right) N_2 \qquad 2.1$$

where the gain coefficient $W_{12}^{2\nu}$ is the two-photon absorption rate, and the loss coefficients (W_{23}^{i}, $W_{21}^{2\nu}$, T_2) are the photoionization, two-photon stimulated emission, and spontaneous decay [41] rates respectively. T_2 is a measure of the total rate of spontaneous emission of the excited state. The branching ratio (BR) of a given transition describes the fraction of atoms in level 2 that undergo spontaneous emission through the given transition relative to all spontaneous emission transitions from the same upper level (which can go to different levels). Based on this, one has that: A2s = T_2*BR, where BR is the branching ratio to the given lower level. A schematic for Eq. 2.1 is shown in Figure 4.

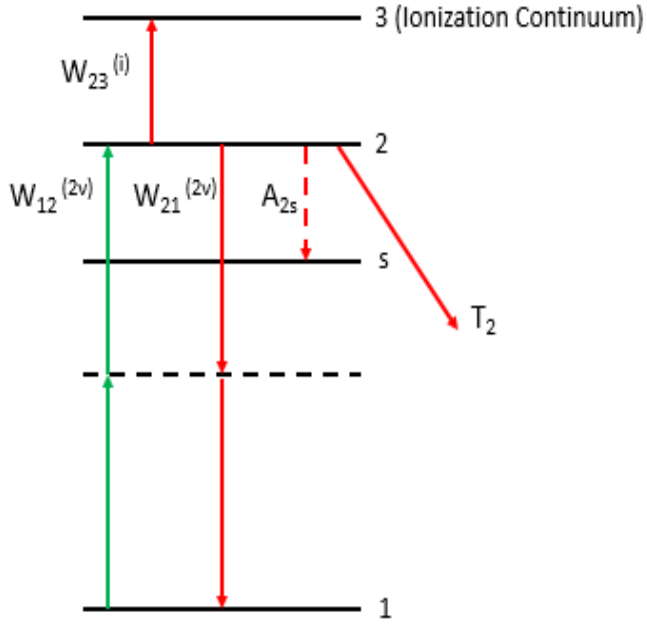

Figure 4: TALIF Level Diagram

We neglect amplified stimulated emission along the beam path (given we do not collect this light with the photodetector). The present assumptions on neglecting collisional excitation, quenching, and amplified stimulated emission follow similar TALIF models developed for other HET and low pressure plasma studies [38], [43]. Additionally, as shown in Table 3, the quenching coefficient (due to collisions with other xenon atoms) for this transition is on the order of 10^{-17} m^3s^{-1}. To calculate a corresponding quenching rate, this value is multiplied by the density of particles in the plasma. For the full range of typical xenon densities found in a Hall thruster plasma (e.g., ~10^{17}-10^{18} m^{-3} from [42]), the quenching rate is orders of magnitude less than the spontaneous decay rate for that transition. A schematic of these gain and loss terms is given in Figure 4. The spontaneous decay rates have been reported [41] and can be calculated from experimental data. The two-photon absorption and photoionization rate coefficients can be calculated from Eq. 2.2 and Eq. 2.3 respectively [38]:

$$W_{12}^{(2\nu)} = W_{21}^{(2\nu)} = \sigma_{12}(I/(h\nu_L))^2 \quad 2.2$$

$$W_{23}^{(i)} = \sigma_i(I/(h\nu_L)) \quad 2.3$$

where σ_{12} and σ_i are the effective cross section for two-photon absorption and the total cross section for photoionization [35], I is the incident beam intensity, and ν_L is the incident laser frequency. The intensity profile is assumed to be Gaussian both spatially and temporally, which is an idealization of the true beam profile. To specify these Gaussians, we use temporal FWHM of 10 ns and spatial FHWM of 1 mm. Because the temporal intensity profile of the laser pulse is not constant, the gain and loss coefficient terms should be treated as time dependent functions. This adds further complexity to the solution to Eq. 2.1, requiring a numerical approach. The effective cross section for TPA can be written in terms of its total cross section in Eq. 2.4 [44]:

$$\sigma_{12} = G^{(2)}\sigma_0^{(2)}g(\Delta\nu) \quad 2.4$$

where, $G^{(2)}$ is the photon statistic factor, for which we take a value of 2 [43]. $\sigma_0^{(2)}$is the total cross section [35] and $g(\Delta\nu)$ is the normalized line profile of TPA. The product of these two values has been reported for the 252.5 nm absorption line [35] but, in general, can be calculated. The line profile can be treated as a convolution of two single-photon spectral profiles and the atom's absorption line profile at the two-photon resonance frequency [43]:

$$g(\Delta\nu) = g_A(2\nu - \nu_A) * g_l(\nu - \nu_l) * g_l(\nu - \nu_l) \quad 2.5$$

where g_A is the two-photon absorption line profile, g_L is the single-photon absorption line profile, ν_A is the two-photon resonance frequency, and ν_L is the single-photon resonance frequency. We approximate that, on the laser centerline, and for the case where the overall broadening is dominated by a Gaussian beam, the line profile can be approximated by Eq 2.6:

$$g(\Delta\nu) = g(0) = \frac{0.66}{\Delta\nu_L} \quad 2.6$$

where $\Delta\nu_L$ is the laser linewidth Full-Width-at-Half-Maximum, for which we use 3.75 GHz. Based on these values, we compute a final cross-section for our experimental conditions of σ_{12} = 4.2 x 10^{-45} cm^4-s

Table 3: Spectroscopic parameters for the rate equation model at 252.5 nm

Spectroscopic Parameter	Value
TALIF total cross-section (σ_0)	2.4 x 10^{-35} cm^4
Photoionization cross-section (σ_i)	3.7 x 10^{-18} cm^2
Total spontaneous decay rate (T_2)	2.5 x 10^7 s^{-1}
Quench rate constant (Q_{2s}) [45]	8.7 x 10^{-23} cm^3s^{-1}

2.2 Comparison of Model with Experimental Data

The model uses absolute signal levels, and signal amplitudes between model and experiment are in quite good agreement (within 10%). In Figure 5, the model and experimental data are plotted with different vertical scales to facilitate comparison of their temporal profiles. The good agreement in this regard provides important model validation. Specifically, the shape of the traces are very similar, exhibiting similar temporal decays with (1/e) time-constants of 51 ns and 45 ns for the experiment and model respectively. The good agreement strongly suggests that the main physical processes are being properly simulated. To obtain an absolute voltage measurement from the experimental TALIF signal one needs to use the relation:

$$V = \frac{\Omega}{4\pi} A L N_2 A_{2s} Q_e \eta R G_{PMT} Q \qquad 2.7$$

where Ω is the light collection solid angle (0.0792 sr), *A* is the cross-sectional area of the measurement volume (8.5 x 10^{-8} m^2), *L* is the length of the measurement volume (as determine by imaged photocathode dimension - 24 mm), Q_e is the quantum efficiency of the PMT (4.8%), η is the collection efficiency calculated by the transmissivity of all optics (80%), *R* is the resistance

used to read a voltage from the PMT current output (50 Ω), G_{PMT} is the PMT gain (3 x 10^5), and Q is the charge of an electron.

Figure 5 shows a comparison (using absolute signal levels) of the signal obtained from the model with a TALIF signal obtained from the helium-xenon buffer gas experiment described in the next chapter.

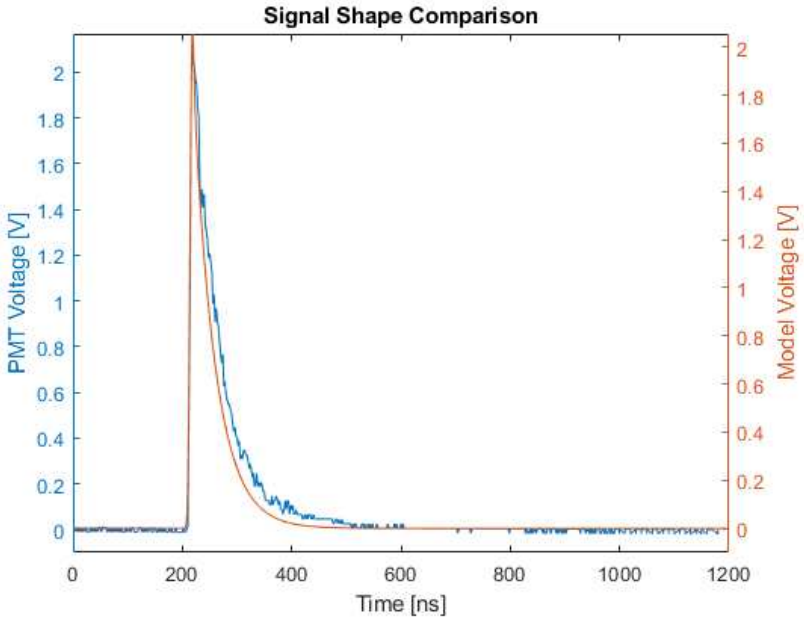

Figure 5: Comparison of TALIF signal model with experiment.

2.3 Signal Calibration Approach for Inferring Density

An approach is required in order to determine (infer) xenon density from measured plasma TALIF signals. Rather than working with only equations, in which case one would need exact values of experimental parameters that can be difficult to determine (e.g., detector gain, solid angle etc.), as well as all rate coefficients (including also collisional excitation and photo-ionization, etc.), we instead follow a calibration-based approach. The calibration is based on recording a calibration curve of experimental TALIF signals at known xenon densities. Then, when TALIF is used on a system with unknown density, and all other experimental conditions are held fixed, the

density can be inferred from the calibration data. Note that fixed conditions include laser parameters such as beam focus size and laser pulse energy. The latter, however, does inherently have some stochastic variation which can by accounted for by normalizing with a photodiode signal that scales with energy.

In regards to the effect of varying temperature on the calibration, note that temperature does not explicitly appear in the equations but enters in the initial condition defining the initial population density of the upper state N_2^0, which is determined by a Boltzmann fraction. The temperature of the neutral particles in the plasma, as defined by their equilibrium velocity distribution, will tend to remain near ambient temperature as these particles are not influenced by the external fields used to generate the plasma. In non-thermal plasma in particular (which HET plasmas are), the ions will also tend toward ambient temperature [9], so the primary means of momentum transfer will also be in thermal equilibrium at ambient temperatures. Therefore, a significant deviation in neutral temperature is not expected. Additionally, velocimetry measurements at the exit plane of a 6 kW thruster report excited state neutral temperatures in the range of 300-800 K, supporting a 300 K approximation in the plume [11], [46]. Given the range of relevant temperatures, the initial (pre-laser) upper-level population N_2^0 is negligible so that temperature effects can be disregarded (except as they relate to initial overall density). For cases where we measure within the nonequilibrium HET plume, there can be some initial N_2^0 population (as also evidenced by background optical emission from these lines) due to electron excitation, but the model presented here captures the optically induced change to the N_2 population (which is what we measure experimentally via background subtraction).

CHAPTER 3: HELIUM-XENON BUFFER GAS EXPERIMENT

3.1 Introduction

Prior to testing in actual plasma devices, i.e. within the plumes of a hollow cathode (Chapter 4) and an HET (Chapter 5), we have performed preliminary tests in a helium-xenon buffer gas mixture as confirmation that TALIF is a viable diagnostic method to assess for application to electrostatic thrusters. The objective was to perform TALIF measurements at sufficiently low densities representative of those required for study of the aforementioned plasma environments. This is an easier, but necessary, step before implementing in the plasma envinroment where additional challenges, in particular plasma optical emission (at similar wavelengths as the detection wavelength), are present. The required density threshold was set by the previously stated objective of achieving a detection limit on the order of 10^{15} m^{-3} or lower. Prior measurements of this type from other members of our research group (as part of earlier Phase I research on the same Air Force funded project) are presented in the Appendix. The remainder of this chapter details buffer gas measurements with focus on understanding and optimizing the signal-to-noise ratio (SNR) of TALIF signals to enable high sensitivity detection (i.e., to minimize the detection limit).

3.2 Experimental Setup

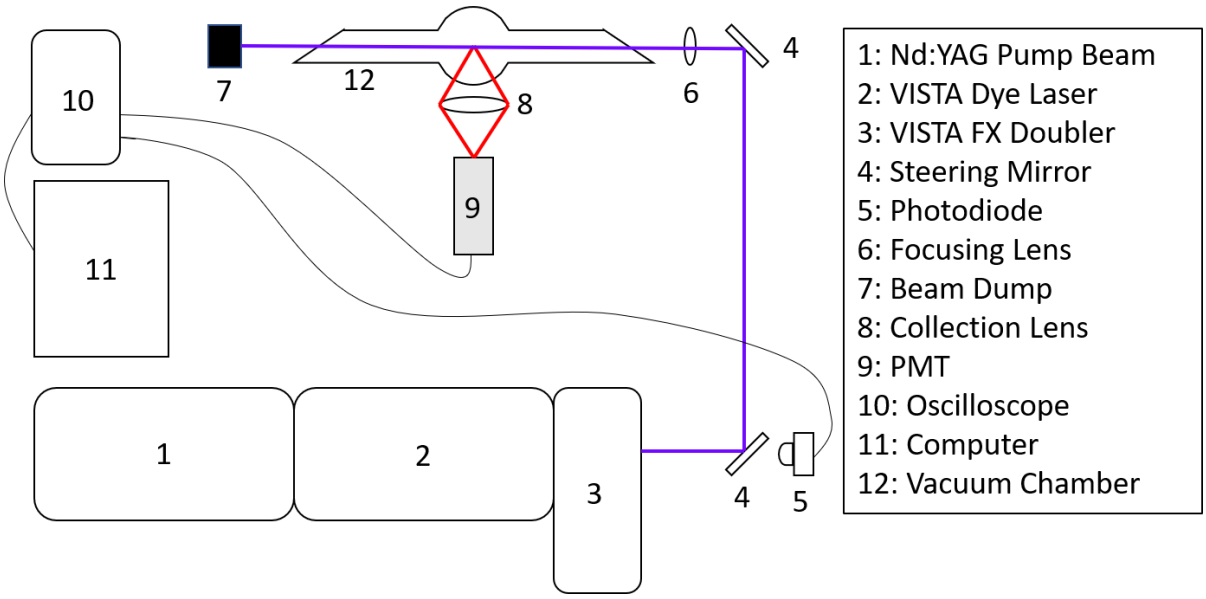

Figure 6: Schematic of He-Xe buffer gas experiment.

Figure 6 shows the experimental setup used for the buffer gas measurements employing a dye laser as the TALIF illumination source. The overall laser system consisted of the third harmonic (355 nm) of an Nd:YAG (Continuum Surelite III) providing a pump beam for the actual dye laser (Continuum Vista). The pump beam was reflected off a mirror (Amplitude Laser 105-0160) at a right angle into the dye laser. The dye (Coumarin 503) was used to generate a visible output beam at either ~499 nm or ~505 nm which was directed to the frequency doubler (Vista FX) to achieve the desired output wavelengths in the vicinity of ~249.5 or ~252.5 nm for the two targeted absorption wavelengths. These wavelengths were selected based on the transitions of Table 2 as well as the preliminary work shown in the Appendix. [Note that the preliminary work employed an OPO laser that could not access wavelengths in the 220 nm vicinity.] The 256 nm line was not tested due to its somewhat reduced strength (product of cross-section and branching

ratio) relative to that of the 249.5 and 252.5 nm schemes [35]. Though the 249.5 nm line has a larger reported strength than the 252.5 nm line, the available PMT's –have higher quantum efficiency at 252.5 nm; therefore, both wavelengths were tested. The wavelength output by the Vista was controlled by a host laptop via the Vista software. A custom LabVIEW code was used to remotely control the host software using RS232 serial communication.

The dye selected was Coumarin 503 (C503), purchased from Luxottica. It has proven a better option than its recommended counterpart Coumarin 500 (C500). C503 is less expensive and requires approximately one fifth the concentration needed to operate the Vista as compared to the C500. Its peak wavelength (505 nm) sits almost directly on the operating wavelengths. Coumarin dyes have an estimated lifetime of 2-4 days according to the Vista laser manual. Thus far, this dye has performed on the lower end of that range. The very short lifetime of Coumarin dyes makes the cost saving characteristics of C503 critical. The doubled beam is capable of achieving a peak energy of ~3.5 mJ at 10 pulses per second with pulse duration of ~10 ns (at wavelengths of ~250 nm). The linewidth varies with the dye concentration selected, but results in section 3.5 show an estimated linewidth of ~13 GHz.

Figure 8 shows a photograph of the vacuum chamber outfitted with a full range pressure gauge (Pfeiffer HPT 200). The chamber was configured with a roughing line (Trivac D30A) but no high vacuum capability. A base pressure of ~15 mTorr (calibrated to air) has been achieved. The input and output of the vacuum chamber have windows cut at Brewster's angle to minimize any reflections. The fluorescent light was detected through a side-mounted collection window (2 ¾" flange). To further reduce noise (stray light scatter), a black tarp and an optical bandpass filter (Edmund Optics 84107 - center wavelength of 832 nm and 37 nm bandwidth) were used to block ambient light from reaching the PMT photocathode. After exiting the dye laser, the TALIF probe

beam was directed by 2 steering mirrors (Thorlabs NB1-K04) through a 500 mm focusing lens (Thorlabs LA4184) into the chamber. Fluoresced light was collected (through the collection window) at an orthogonal collection angle with an uncoated plano-convex lens (diameter 1") of focal length 40 mm (Thorlabs LA1422) that was positioned 80 mm from both the collection region and photomultiplier detector (i.e., 1:1 magnification imaging). In this way, fluorescence was collected from a measurement volume along the TALIF probe beam with length equal to the extent of the PMT photocathode. Two photomultiplier tubes were (alternately) used in this experiment (Hamamatsu R3896 and Thorlabs PMT1001) in order to compare their performance. The R3896 has an 8 mm x 24 mm photocathode, and the PMT1001 has a circular diameter of 8 mm. The Hamamatsu R3896 PMT was available and used for preliminary studies, and the Thorlabs PMT1001 was purchased for its higher quantum efficiency at both operating wavelengths.

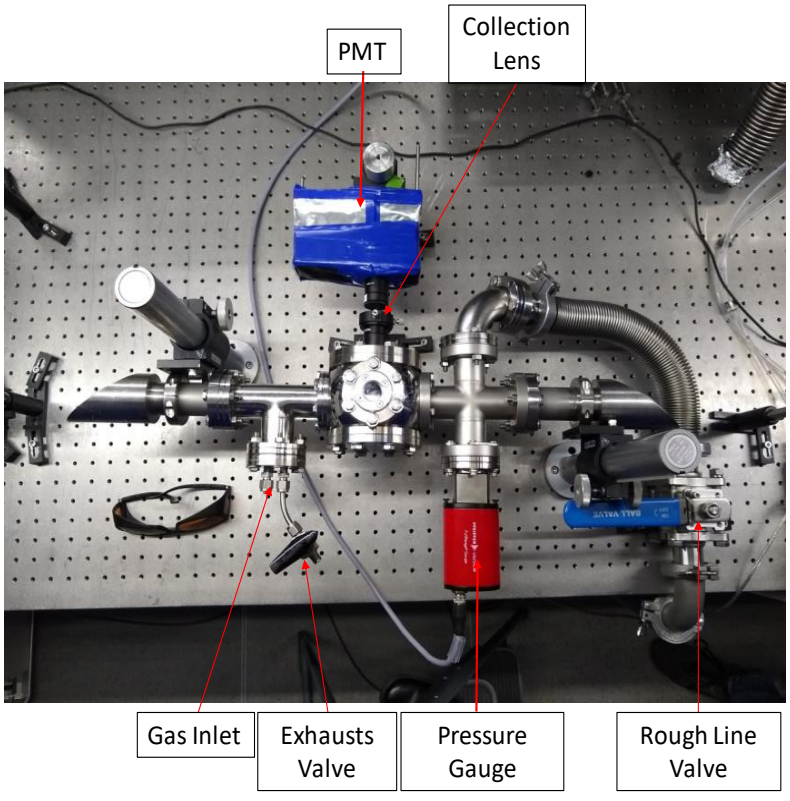

Figure 7: Experimental setup for buffer gas measurements.

A photodiode was placed behind a steering mirror (not shown) for triggering (of data acquisition) and to normalize TALIF signals against beam energy. The signals, i.e., the temporal voltage waveforms $V(t)$ due to each laser pulse, from the PMT and photodiode were sent to an oscilloscope (Tektronix TDS5034B), the output of which was passed to a personal computer controlled by the LabVIEW data acquisition code to receive signals averaged over 100 laser shots. Wavelength was monitored using a wavemeter (High Finesse WS5) with precision of 0.001 nm. At each wavelength position, the (average) recorded PMT and photodiode signals (traces) were first baseline subtracted to remove the effects of any background signals or dark currents. This subtraction was performed (in post-analysis) by fitting a single line (linear segment) to the signal on either side of the peak, and subtracting the values of this line from the raw data. After subtraction, the PMT trace was inverted in order to work with positive values, and trapezoidal integration was used to determine the area under each trace. An example of baseline subtraction and area determination is shown in Figure 8. The ratio of the PMT signal area to the photodiode signal area is recorded as the TALIF signal (i.e., a linear normalization is performed).

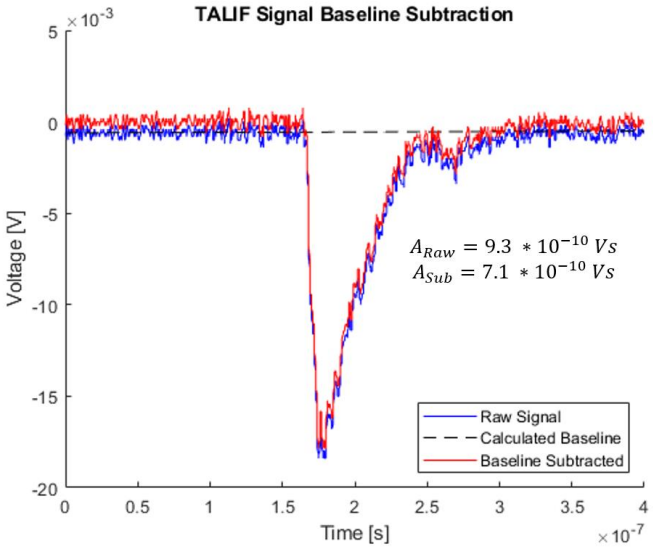

Figure 8: PMT signal showing background subtraction and area determination.

The buffer gas tests involved measuring TALIF signals at different fixed (and known) xenon concentrations within the small vacuum chamber. The gas concentrations were set (and determined) by first evacuating the chamber, then filling it with a helium-xenon buffer gas (10 ppm xenon in balance of He) to a total pressure of ~1 torr to achieve concentrations at roughly the target levels. This case corresponds to a number density of xenon of 3.25 x 10^{17} m^{-3} (assuming a temperature of 300 K). To achieve other (lower) densities, the pressure is further reduced by opening the valve to the vacuum pump line. At each pressure level, the valves to the roughing line and gas inlet were closed so the chamber remained at a fixed, uniform pressure and TALIF data was recorded. (We have verified that leaks did not significantly change the chamber pressure during the measurement intervals.) Also, for (only) these measurements there is a small unexplained background PMT signal (i.e., TALIF channel) even in the absence of xenon with a similar temporal signature. This signal is assumed to be constant over the series of experiments, likely due to other pulsed luminosity, and was subsequently subtracted from the other signals, i.e., from the TALIF signals for the experiments using xenon. One potential source of this signal is stray light from the flashlamps in the pump beam laser. The effect of this subtraction is quite small given that the background signal has an area equivalent to Xenon at concentration of ~10^{16} m^{-3}, whereas measured concentrations are in the 10^{17} m^{-3} range.

3.3 Results of TALIF Buffer Gas Experiment

3.3.1 TALIF Absorption Spectra

Absorption spectra, i.e., the LIF signal as a function of the laser excitation wavelength, provide a powerful tool for examining TALIF signals. The ability to sweep the beam wavelength helps mitigate possible wavelength instability concerns and, depending on the laser linewidth, the width of the measured TALIF peak can provide information about which broadening mechanisms

dominate. Under the right conditions, line broadening analysis may be used for velocity measurement through Doppler shifts or temperature measurements through Doppler broadening. Additionally, for fixed experimental conditions (laser power etc.), the LIF signal (amplitude or area) scales linearly with xenon concentration, so density measurements based on a calibration method can be performed. Typically, recording a single absorption scan based on 100-shot averages over 50 wavelength steps requires approximately 15 minutes to complete. (Scan times for the 10 pulses-per-second laser would be a bit faster, but there is some latency associated with the real-time data acquisition and processing). Given the rapid decomposition of the Coumarin dye when the laser is operating, the laser energy tended to drop by ~1 mJ (~30-50% of the starting energy) over the course of a given absorption scan. For this reason, the photodiode energy normalization is employed (assuming LIF signals depend linearly on laser energy as is further examined in Chapter 4).

The data in Figure 9 compares TALIF absorption spectra for 4 configurations, i.e., for absorption at ~249.5 versus ~252.5 nm, and for PMT R3896 and PMT1001, all at similar xenon concentration. The concentrations were not precisely controlled because a mass flow controller was not installed on the chamber. It is also important to note that the two PMTs operate on different voltage scales, so their signal amplitudes are not directly comparable. To compare performance of the 4 combinations, the signal-to-noise-ratio, SNR, where the signal is defined as the peak of the spectrum (fitted with a Gaussian) and the noise as the standard deviation of the baseline, is used. The resulting values of SNR for the four cases (R3896 at 252.5 nm, PMT1001 at 252.5 nm, R3896 at 249.5 nm, and PMT1001 at 249.5 nm) are 5.7, 2.4, 110, and 24 respectively. These observations are reasonably consistent at other xenon concentrations (as long as the PMT is not saturated etc.), leading to the conclusion that the optimal signal can be acquired using the R3896 PMT at a laser

wavelength of 249.5 nm. Furthermore, there are additional concerns when using the PMT1001 in terms of apparent "after-pulses" which inhibits accurately capturing the exponential decay of the TALIF signal.

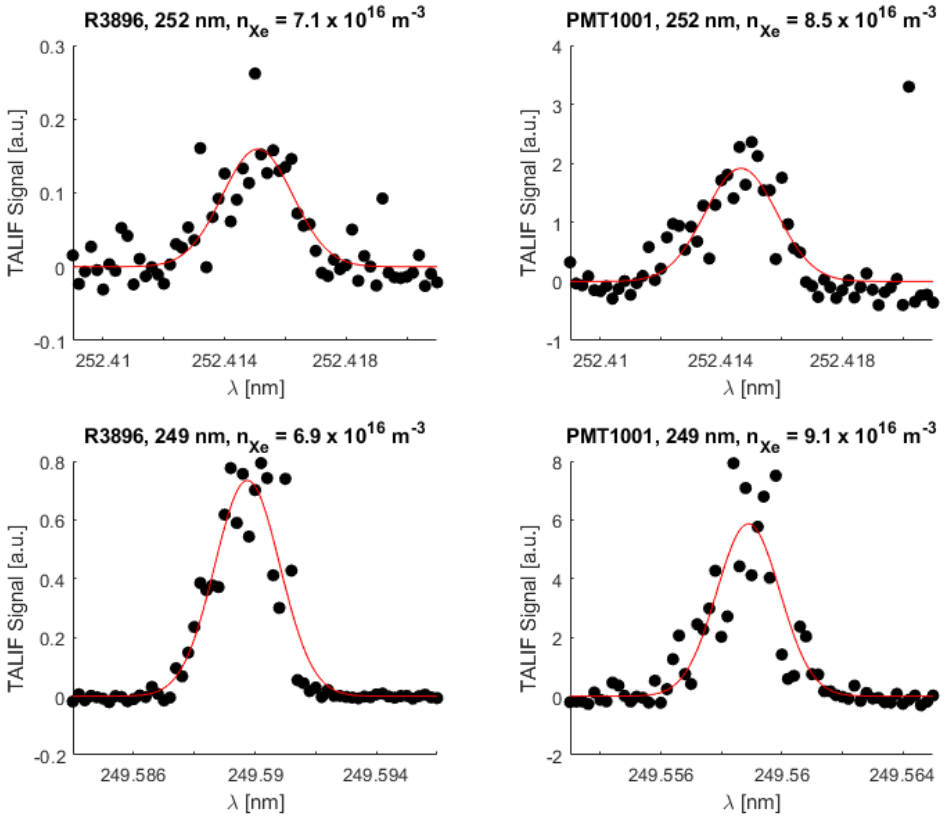

Figure 9: TALIF absorption lines for 4 different configurations of transition wavelength and PMT selection.

Because the chamber was configured only for rough vacuum, it cannot reach sufficiently low pressures to directly access the targeted lower xenon detection limit (given also the available Xe gas mixtures). However, the TALIF signal varies linearly with Xe concentration, so scaling the peak signal amplitude by the inverse of the SNR provides an estimate of the lowest concentration at which a peak can be expected to be resolved (and is a common method for estimating detection limit). Specifically, the data for R3896 PMT and 249.5 nm (bottom left plot in Figure 9) have

SNR of ~110 for a Xenon concentration of 6.93 x 10^{16} m^{-3} yielding an expected detection limit of ~6 x 10^{14} m^{-3}. This limit is in the correct order of magnitude relative to the requirement of ~10^{15} m^{-3} and is roughly consistent with earlier preliminary experiments.

3.3.2 TALIF Signal Dependence Versus Xenon Concentration

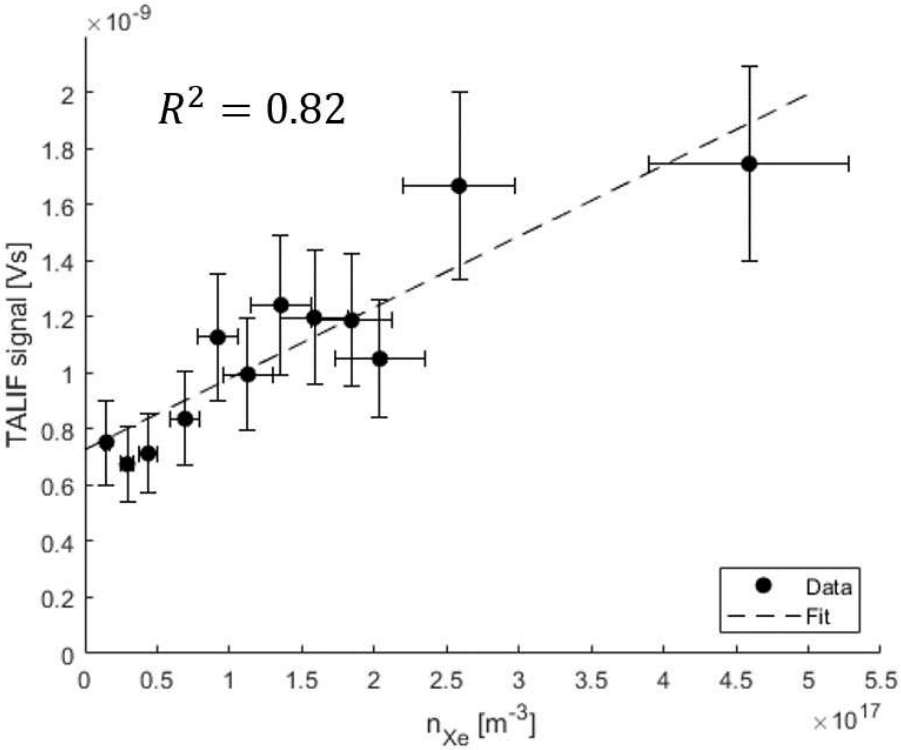

Figure 10: TALIF signal as a function of xenon concentration.

The previously mentioned assumption of the TALIF signal scaling linearly with xenon concentration is critical for measuring unknown Xe concentrations using a calibration approach. Figure 10 shows TALIF signals recorded using the setup from Figure 6for a range of xenon densities ranging from 0.15 – 4.60 x 10^{17} m^{-3}. The different densities were achieved by varying the chamber base pressure (and using the Ideal Gas Law as discussed earlier). These data were recorded with the laser fixed at the peak absorption wavelength of 249.589 nm. The stability of

the laser to remain at this wavelength was monitored using the wavemeter and was determined to be stable within ±0.001 nm over the course of experiments. In the plot, error bars (uncertainty) for TALIF signals are found as 20% (given the results in section 3.3.3) while those for (expected) number density are estimated to be 15% based on uncertainty in the pressure measurement system. The data exhibits the expected linear trend ($R^2 = 0.82$); however, the trend line intercept does not pass near the origin as it should. This deviation is largely attributed to chamber pressure measurement uncertainty and possibly the background signal issue mentioned above in Section 3.1, though this hasn't been directly proven.

3.3.3 Single-Shot TALIF Signal Variation

As an additional check to verify the optimal measurement configuration and to examine the possibility of single-shot measurements (time resolution of ~100 ns), the shot-to-shot variation of the TALIF signal is recorded. The capability for single-shot measurements would be very interesting to provide higher time-resolution data, e.g., to possibly resolve plasma fluctuations or instabilities, which are lost (averaged-away) in the multi-shot averages. The single-shot data also provides a measure of the error associated with every averaged TALIF signal. In three of the cases, shown in Figure 11, the standard deviation about the mean sits near 20% (fairly independent of which PMT is being used), which is used as a representative value of uncertainty (error bars) for the reported TALIF measurements.

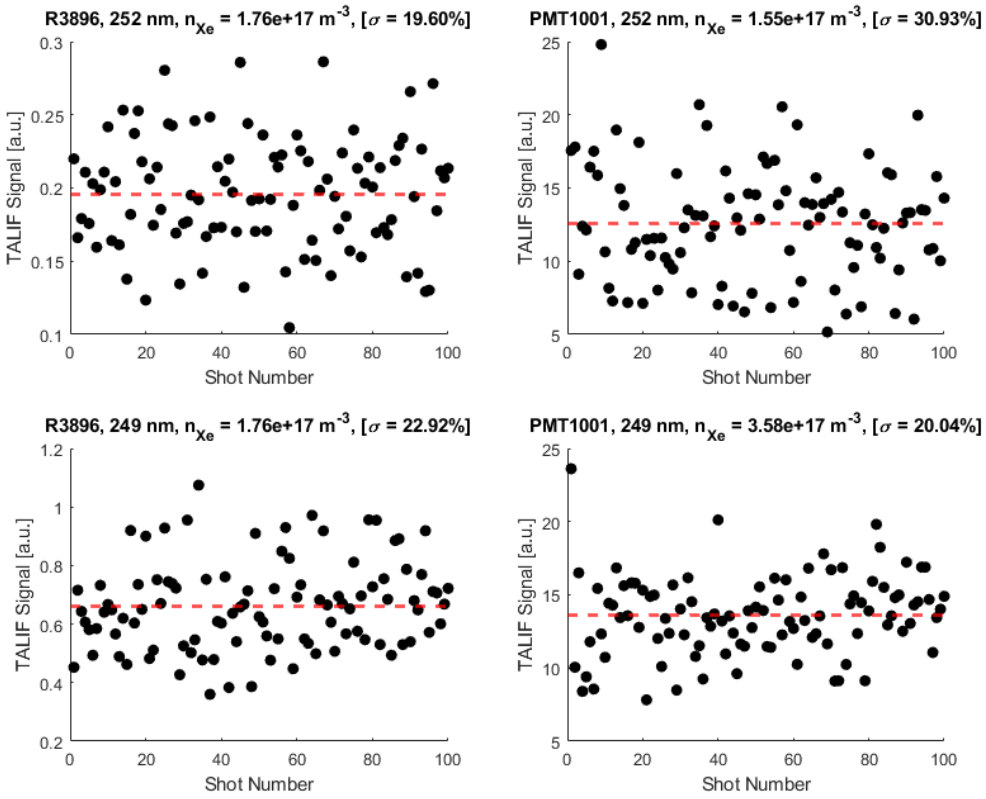

Figure 11: Shot-to-shot TALIF variation

CHAPTER 4: BARIUM OXIDE HOLLOW CATHODE EXPERIMENTS

4.1 Introduction

The buffer-gas vacuum chamber experiments described in the previous chapter served to validate the basic diagnostic configuration. The results provided a useful measure of signal strength and confirmed the basic spectral scheme, but they did not take into consideration optical emission from the plasma which is expected to be a primary physical mechanism limiting TALIF detection capability in plasma environments (i.e., competing plasma luminosity at the TALIF emission wavelengths). The present chapter details a set of experiments performed in a high vacuum chamber (~1 x 10^{-6} torr base pressure) within the plume of a barium oxide (BaO) hollow cathode. As discussed herein, these results are useful in terms of examining TALIF signals from plasmas with particular emphasis on plasma background luminosity.

The electrons, ions, and neutral atoms in the plasma constantly undergo a series of processes including ionization, recombination, excitation, and de-excitation. Among these, radiative de-excitation of electrons bound to the nucleus of (excited) atoms and ions are the primary source of light emission. This process of light emission gives the plasma its vibrant color and also allows diagnostics based on optical emission spectroscopy [47]. With regard to TALIF measurements, the plasma optical emission is also collected by the PMT thereby providing a background signal (interference) to the TALIF. As discussed below, spectral filtering can be used to suppress the emission which, if it is too strong, can add significant noise to the TALIF measurements (or otherwise complicated the measurements, for example by saturating the light detector). In terms of the temporal signature, the optical emission tends to be present at all times whereas the TALIF signal is pulsed and coincident with the laser. Given this different time

dependence, the emission background can nominally be "subtracted off" without issue (as PMTs collect light in an additive way). However, in practice, PMTs have a limit on the amount of light they can receive before their response distorts or saturates (owing to issues with current flow through the resistor chain). In the present work, the R3896 PMT is rated to handle a continuous (DC) anode-current draw of maximum 0.1 mA (5 mV when viewed with 50 Ω impedance on scope). The background light emission can also place a limit on the PMT gain setting, which can reduce SNR. Therefore, one generally seeks to both maximize TALIF signal strength and minimize the amount of background emission being collected. Unfortunately, the TALIF lines also tend to be strong plasma emission lines (i.e., from the same transitions), meaning that any spectral filtering tends to affect both the desired TALIF signal and the background emission. These issues are examined below.

4.2 Experimental Setup for Hollow Cathode Measurements

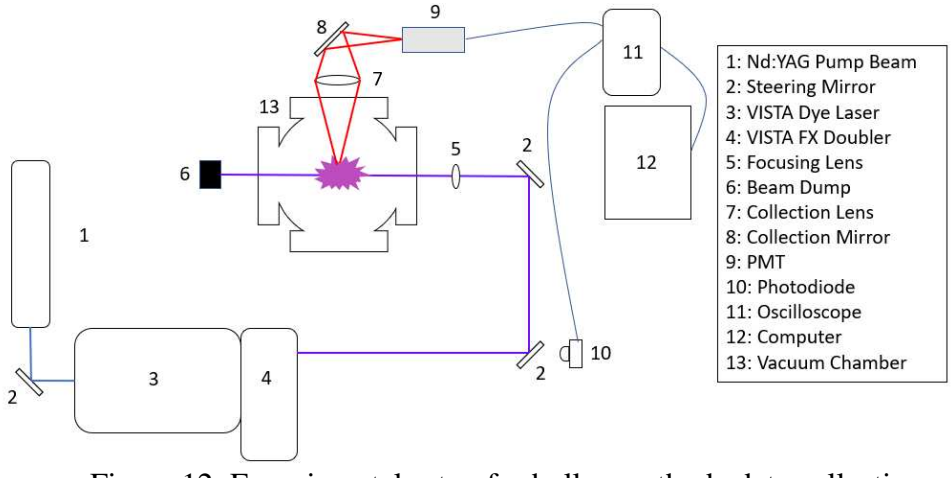

Figure 12: Experimental setup for hollow cathode data collection

The schematic shown in Figure 12 shows a similar experimental setup to Figure 6 in Chapter 3. In this case, the beam exited the frequency-doubler and was directed by steering mirrors

(Thorlabs NB1-K04, later changed to Lattice Optics RX-225-45-UF-1025 after wavelength change) into a vacuum chamber (~ 61 cm x 61 cm x 61 cm) that was equipped with a turbomolecular pump (Agilent TV1001). Prior to entering the chamber, the beam passed through a 750 mm uncoated focusing lens (Thorlabs LA4716) to loosely focus the beam at the measurement region (beam diameter ~2 mm). A pair of steering mirrors in a periscope configuration (not shown) is used to bring the beam up to the height of the chamber input window. The input window (ThorlabsVPCH42-UV) was AR coated and designed to be bolted to a 7 cm flange with a copper gasket seal. The focal distance was increased from 500 mm (in buffer gas tests) to 750 mm to accommodate the increased chamber size and added path length due to the periscope mirrors. The beam exited through an output window (ThorlabsVPCH42-UV) and into a beam dump. The TALIF signal was collected by a 5.1 cm diameter AR coated lens with a focal length of 150 mm (Newport KBX160AR.16). To maintain 1:1 magnification, the lens was placed 300 mm away from the beam focus, just outside the chamber window (uncoated). To keep the collection optics within the dimensions of the optical table, the light collected by the lens was turned with a 5.1 cm mirror (Thorlabs BB2-E03) towards the PMT. As before, the oscilloscope was triggered by a photodiode placed behind a steering mirror, and the photodiode signal was used to normalize the TALIF signal against beam energy variation. The assumption of linearity between TALIF and laser beam energy that is required for the normalization method is validated later in this chapter (Section 4.4).

A barium oxide (BaO) hollow cathode was centered in the chamber with the keeper orifice plate ~ 1 cm above the beam focus. The cathode was operated with a keeper voltage of 600 V and current of ~0.5 A. The anode voltage was typically ~35-45 V with current ~6-10 A. The anode operation was current limited and the keeper was voltage limited. However, the keeper voltage

was fixed at 600 V in the work reported here. Xenon gas (99.999%) was fed through the center of the cathode via a digital mass flow controller (Unit Instruments 7360) with flow rates ranging from 5-15 sccm.

Plasma Emission Studies – Wavelength Selection

To get an understanding of the expected background signal due to optical emission, a compact fiber-coupled spectrometer (Ocean Optics HR4000) was used to view the cathode plasma through a chamber window (with no other collection optics). The spectrometer was calibrated for wavelength response but not amplitude response. The plasma was generated with the cathode operating at 6 A and a gas flow of 5 sccm. Figure 13 and Figure 14 show survey spectra of plasma emission from the overall cathode region, with the latter showing a zoomed-in region near the target 828 nm TALIF detection wavelength. The emission spectra reveal multiple emission lines that may be problematic for TALIF detection. In the visible region from ~400–600 nm, there is a broad group of emission lines, most of which can be attributed to singly ionized xenon. In the region of ~600-1100 nm, there are many lines including some in the vicinity of the TALIF detection wavelengths. Also notable is a strong neutral xenon emission line just above 880 nm.

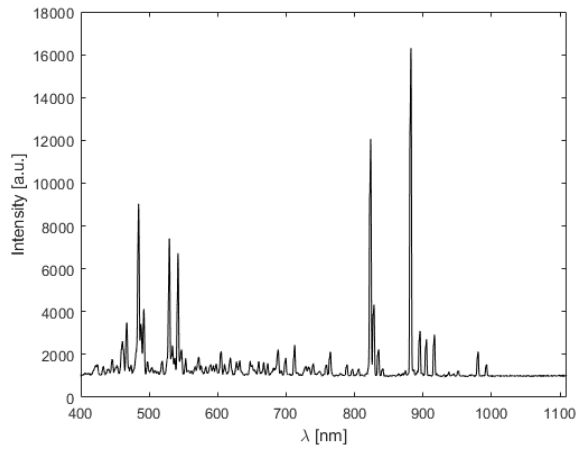

Figure 13: Emission spectrum from cathode operating on Xenon.

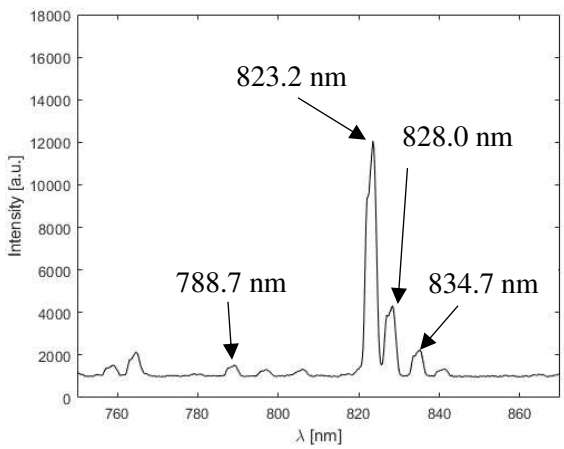

Figure 14: Zoom-in of emission spectrum from cathode operating on Xenon

Given the potential interferences, several filtering schemes were investigated. First, a bandpass filter (Edmund Optics 84107) with a center wavelength at 832 nm and a FWHM of 40 nm was placed in front of the PMT to block light from lines outside of the filter passband. However, this filter cannot effectively block the emission from the three lines that were considered for TALIF detection (823.2, 828.0, and 834.7 nm) shown in Figure 14. The 823.2 nm line acts as the largest source of background emission. The selected TALIF setup (249.5 nm beam) fluoresces at 828.0 nm such that, ideally, light from the 823.2 and 834.7 nm lines would be strongly filtered; however, the close proximity of the lines to one another posed a technical challenge in terms of spectral characteristics of available filters. A longpass filter (Edmund Optics 86-070) with a cut-on wavelength of 825 nm, was added in front of the bandpass filter (mentioned above) in order to reduce the measured background emission from the 823 nm line. While the targeted emission appeared to have been suppressed given the reduction in peak strength from ~12,000 in Figure 14 to ~1,800 in Figure 15 (with the same collection settings), the remaining (unblocked) emission still generated too large of a signal to reliably operate the PMT (based on current limits). Figure 16 shows the plasma background signal exceeding the 5 mV threshold at the PMT minimum operating gain voltage setting of 500 V (~10^2 gain). Operating in this way would lead to saturated PMT signals (may become non-linear or distorted) and the addition of simple neutral density filters (to reduce all light) is also problematic given the reduction in TALIF signal that would be introduced (eventually causing the TALIF signal to fall into the noise-floor of the detector). The conclusion then was that this experiment cannot be performed with this configuration within the xenon plasma at the 252.5 or 249.5 nm laser wavelengths. Indeed, we have found no existing literature that details TALIF measurement in a Xe plasma using either of these two wavelengths.

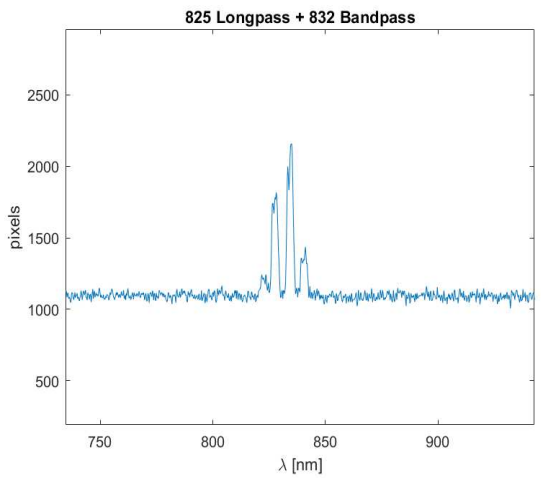

Figure 15: Xenon spectrum with bandpass and longpass filter (see text).

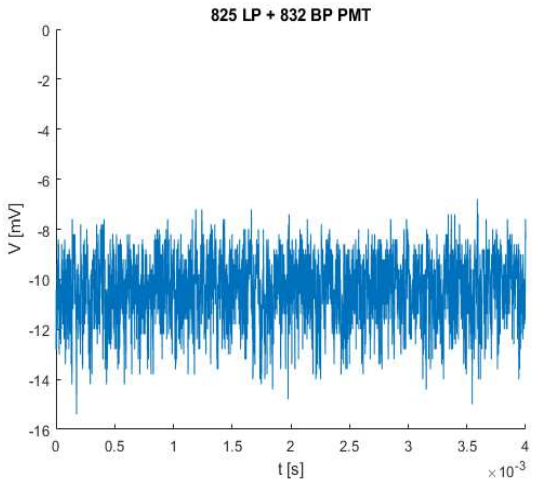

Figure 16: PMT signal due to cathode plasma with bandpass and longpass filter (see text).

The two TALIF lines studied thus far were motivated in part by the limitation of the available OPO laser (used also in our group's earlier work shown in the Appendix) to reach the 22X nm wavelengths. However, a dye laser that was later available for the project can access these lower wavelengths. A review of existing research has shown that for any TALIF performed in a xenon plasma, neither the 252 nor 249 nm line has been used. Instead, researchers have employed the 222.5 or 224.5 nm lines [42], [48], [49]. This finding is also not surprising in light of their high cross-sections and branching ratios (Table 2) combined with the relatively weaker plasma emission present at their associated emission wavelengths (i.e., 788.7 nm emission for 222.5 nm excitation; 834.7 nm emission from 224.5 nm excitation), as can be seen in Fig. 14. For the remaining work in this thesis, the 222.5 nm line (788.7 nm emission) was selected over the 224.5 nm line (834.7 nm emission) owing to its weaker plasma background emission (as observed in our experiments) combined with a comparable cross-section (and branching ratio), all of which leads us to expect better SNR for this line. For operation at 222.5 nm, Coumarin 440 was used as the

dye and a new bandpass filter (Thorlabs FB790-10), centered at 790 nm with FWHM 10 nm), was placed in front of the PMT. (This is the only PMT filter used in this scheme.)

As a preliminary test of the new setup, conditions mimicking the Chapter 3 buffer gas experiment were established using a glass cell filled with a He-Xe buffer gas at 10 ppm Xe with pressure 1.52 torr. The TALIF signal was compared with earlier results at similar concentrations, optical collection setup, and beam energies. The results, shown in Figure 17, verify the transition to a new wavelength setup has not resulted in a dramatic loss in TALIF signal strength. Based on the emission interferences described above, the new 222.5 nm scheme can thus be reasonably expected to perform better than 249.5 nm for measurements in plasma environments.

At similar laser pulse energy and xenon concentration, the TALIF signal at 222.5 nm is larger (at its peak) than that from 249.5 nm excitation by a factor of ~1.6. The ratio of 1.6 is roughly as expected based on cross-section and branching ratios; there may also be a weak effect of reduced transmission of 222.5 nm light through the chamber window. The new 222.5 nm scheme was also

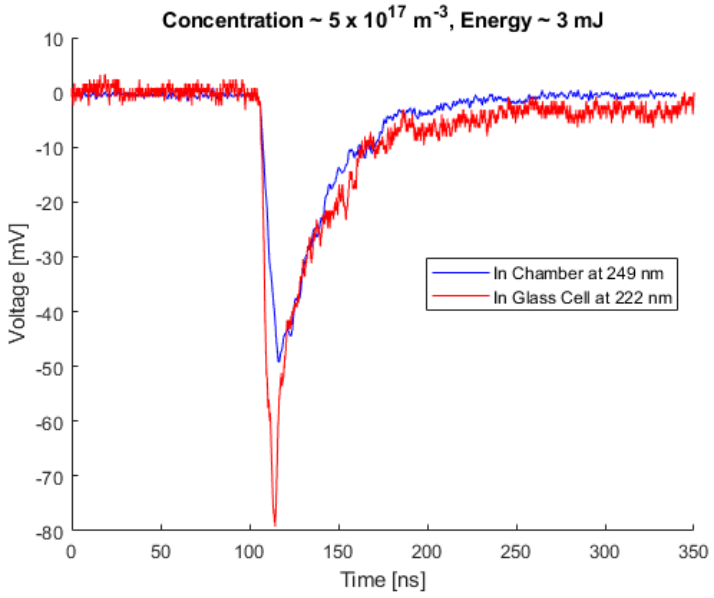

Figure 17: Comparison of buffer gas TALIF using 249 nm (blue) and 222 nm (red) wavelengths.

tested in the hollow cathode plasma and a distinguishable signal was recorded. From this point on, the 222.5 nm line was used for all TALIF data.

4.3 Dependence of TALIF Signal on Laser Energy

The different processes involved in TALIF signal generation (Chapter 2) have different energy dependences, e.g., the two-photon absorption step scales with the square of the incident beam intensity, meaning there may be a complex non-linear relationship between the TALIF signal and beam energy. Here, measurements of this TALIF-energy dependence were conducted to support the (linear) photodiode normalization technique used throughout this work. Measurements were conducted for a cold-flow of xenon gas through the cathode inlet at flow rate of 5 sccm with the PMT operating at the same 500 V gain setting used throughout this chapter. The experiment was performed immediately after mixing fresh dye to obtain the maximum energy output (typically ~ 2.5 - 3mJ). At each energy setting, 100 averaged shots are recorded. The energy was gradually decreased by rotating the BBO frequency doubling crystal in the VISTA FX Doubler unit. There was no observable beam steering as a result of this rotation, so the location of the measurement volume within the gas flow remained fixed.

In Figure 18, both the recorded TALIF signal peak and integrated area are plotted against beam energy for energies ranging from ~0.25–2.5 mJ. The TALIF signal based on the peak corresponds to holding the laser fixed at the measured peak wavelength of 222.506 nm, whereas the area measurement corresponds to the integrated area under the voltage trace. As can be seen in Figure 18, both analysis methods yield TALIF signals that vary linearly with beam energy, each having R^2 values of 0.99. While, from theoretical grounds, it is not clear that the linear dependence holds over larger energy ranges, other published research [42] supports the use of a linear dependence at low energies. In the Appendix, we also provide a plot of TALIF signal versus laser

energy from the model which supports the assumption of a linear dependence at the low beam energies used in the current work.

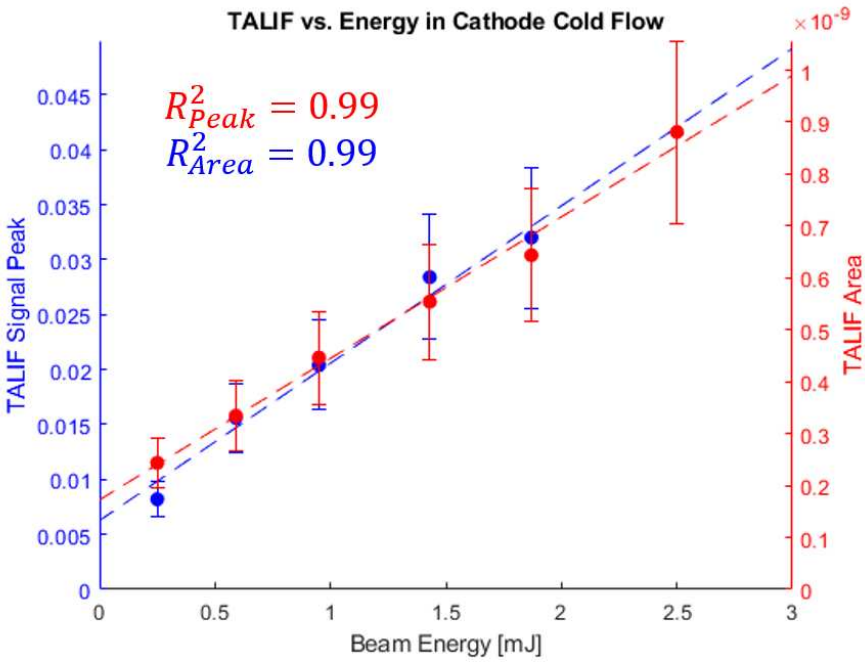

Figure 18: TALIF signal peak and integrated area as a function of beam energy

4.4 TALIF Study of BaO Hollow Cathode

4.4.1 Variation of Anode Current

A series of TALIF studies was performed on the hollow cathode to characterize the TALIF method (in preparation for Hall thruster measurements) and to gain possible insight into the physics of the hollow cathode operation. The same setup of Figure 12 was used though with the laser set for 222.506 nm excitation, detection at 788.7 nm, and the single CWL 790 nm bandpass filter on the PMT as detailed in the section above. This subsection examines variations in in anode current while upcoming subsections examine effects of variation in flow rate and radial measurement position.

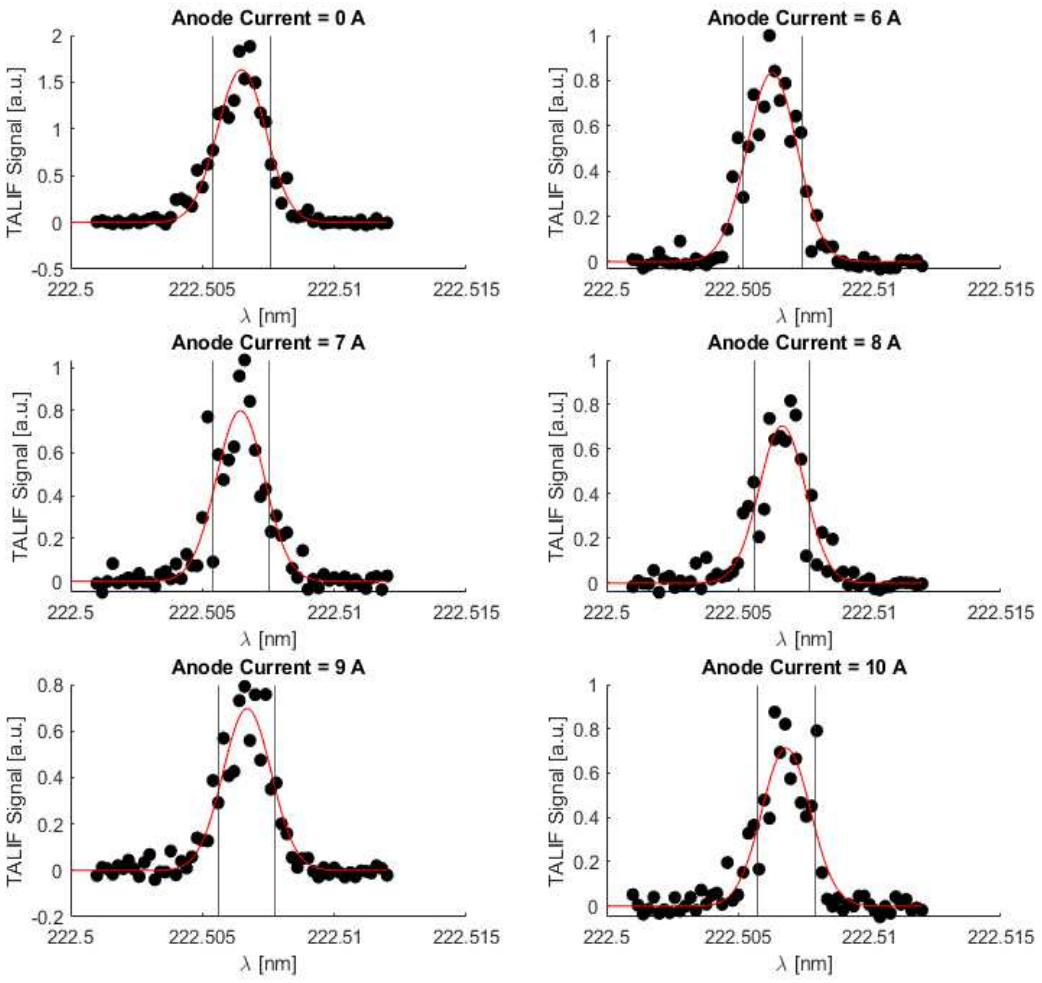

Figure 19: TALIF absorption lines at anode currents of 0, 6, 7, 8, 9, and 10 A. (The zero current case corresponds to the cathode being off.) Data is background subtracted and fit by a Gaussian profile. Vertical black lines indicate the FWHM for each peak.

The study on anode current variation employed a flow rate of 5 sccm corresponding to an operating pressure of 2 x 10^{-4} torr. The keeper voltage and current were set as previously described and the anode voltage varied freely as the anode current was adjusted in the range of 6-10 A (with 1 A steps). The laser was scanned over the 222.5 nm TALIF feature with 100 TALIF signals averaged at each wavelength step. The resulting TALIF absorption spectra shown in Figure 19 were recorded in steps of 0.002 nm. Data was also recorded with the cathode off (i.e., an anode

current of 0 A). For all measurements, the PMT gain was set to its minimum specified setting of 500 V.

As shown in Figure 19, the TALIF spectrum (in particular peak value) has very little variation over the range of anode currents studied when the cathode is operating (i.e., for all currents except 0 A), meaning there is minimal variation of xenon neutral density. This is expected due to the low propellant utilization efficiency of hollow cathodes. The analogous experiment was repeated for flow rates up to 15 sccm in 2.5 sccm steps (with amaximum operating pressure of 7.8 x 10^{-4} torr) and yielded similar results. The ~ 50% drop in signal from the 0 A case to all other cases is primarily due to an increase in neutral temperature, likely with a smaller contribution due to ionization. Typically hollow cathode ionization fractions are < 10% [50], [51], while the neutral gas temperature in a hollow cathode insert is relatively high at ~ 1500 – 2000 K [50], [52], [53]. The neutral gas temperature downstream of the keeper orifice may be expected to decrease as the gas expands, but should be of magnitude to account for the large drop in signal due to the effect on starting density, i.e., density scales inversely with temperature at fixed pressure (under the ideal gas approximation).

4.4.1.1 *Analysis of Linewidth of TALIF Spectra*

In some cases, the spectral shape of absorption lines (i.e., laser wavelength scans of TALIF) can provide particle velocity or temperature information via a change in their linewidth due to Doppler broadening. A Doppler shift is a relativistic effect in which the frequency of light as detected by an observer will shift up if the light source is moving toward the observer, and down when moving away [54]. Assuming the particles are moving in all directions as described by a Maxwellian distribution, the range of light frequencies absorbed by the xenon atoms will increase,

with both higher and lower frequencies contributing, which would result in a broadening of the collected wavelength spectrum. Because the velocity scales with temperature, the resulting "Doppler linewidth" assumes a temperature dependence as given by Eq. 4.1 [55]:

$$\delta\nu_D \cong \nu_0 * \left(7.16 * 10^{-7} \sqrt{\frac{T}{M}}\right) [Hz] \tag{4.1}$$

where $\delta\nu_D$ is the Doppler linewidth, ν_0 is the resonant frequency, T is the temperature in Kelvin, and M is the atomic mass of the atom in amu [55]. In this experiment, at an estimated neutral temperature of 300 K, the Doppler width would be 1.4 GHz. Figure 19 shows a linewidth of 13.1 ± 0.5 GHz in all cases which is considerably broader than the postulated Doppler broadening. The key point is that the observed broadening is due to a combination (convolution) of effects including Doppler broadening, collisional (pressure) broadening, natural broadening, and the contribution of the laser itself. Finally, any hyperfine or isotopic structure of the spectra should also be considered. Xenon has 9 stable isotopes, with 7 among them having a relative abundance greater than 1% [26]. These isotopes each have their own sets of electron energy levels, shifted relative to one another by the varying mass of the nucleus. Additionally, 2 of the 9 stable isotopes have an odd number of nucleons, allowing for a net non-zero nuclear spin and causing what is known as nuclear spin splitting of energy levels. In the present case, natural broadening is very narrow (~ 2.2 MHz as given by $A_{2s}/2\pi$ [56]) and collisional broadening is very low (<~MHz) at these vacuum pressures (see Section 1.3.6). Though the hyperfine structure of the 788.7 nm emission line has not been fully characterized, typical xenon hyperfine splittings of other xenon excitation levels result in broadening on the order of 100 MHz [25], [57], meaning they are likely not the dominant mechanism in the observed 13 GHz signal linewidth.. Although a full analysis has not been performed, it appears that the observed width of the TALIF lines is dominated by the laser

linewidth which is reported in the datasheet to be ~ 1.5 GHz but is subject to increase with errors in beam alignment and dye concentration. Dye concentration may be investigated more thoroughly in the future in an attempt to decrease the observed TALIF linewidth closer to its optimal value. More research on the line broadening will be conducted in future work.

4.4.2 Variation of Cathode Flow Rate

Here, variation of the TALIF signal with cathode flow rate was examined. Because changes in flow rate cause variation in the chamber pressure, and thus xenon density, the TALIF signal is expected to vary with flow rate. Of course, any changes in ionization fraction (between conditions) will also impact the final neutral density. The experimental procedure was nearly identical to that described in section 4.5.1; however, in this case the current was fixed at 8 A and the flow rate varied from 5 sccm to 15 sccm in 2.5 sccm steps, resulting in the chamber pressure varying from 2 - 7.8 x 10^{-4} torr as read by the full range pressure gauge. Additionally, results reported here are based on the amplitude (at peak wavelength) of the TALIF spectrum versus its area (with earlier results showing equivalence of these methods) using 100 shot averages.

Results of the TALIF measurements at varying pressure for several different axial positions (downstream of the cathode central axis but on center line) are shown in Figure 20. Each plot shows a linear fit given the expected linear dependence of TALIF signal on chamber pressure (neglecting ionization and assuming the pumping does not introduce spatial non-uniformity in xenon density). In most cases, the observed trends are fairly linear based on R^2 values.

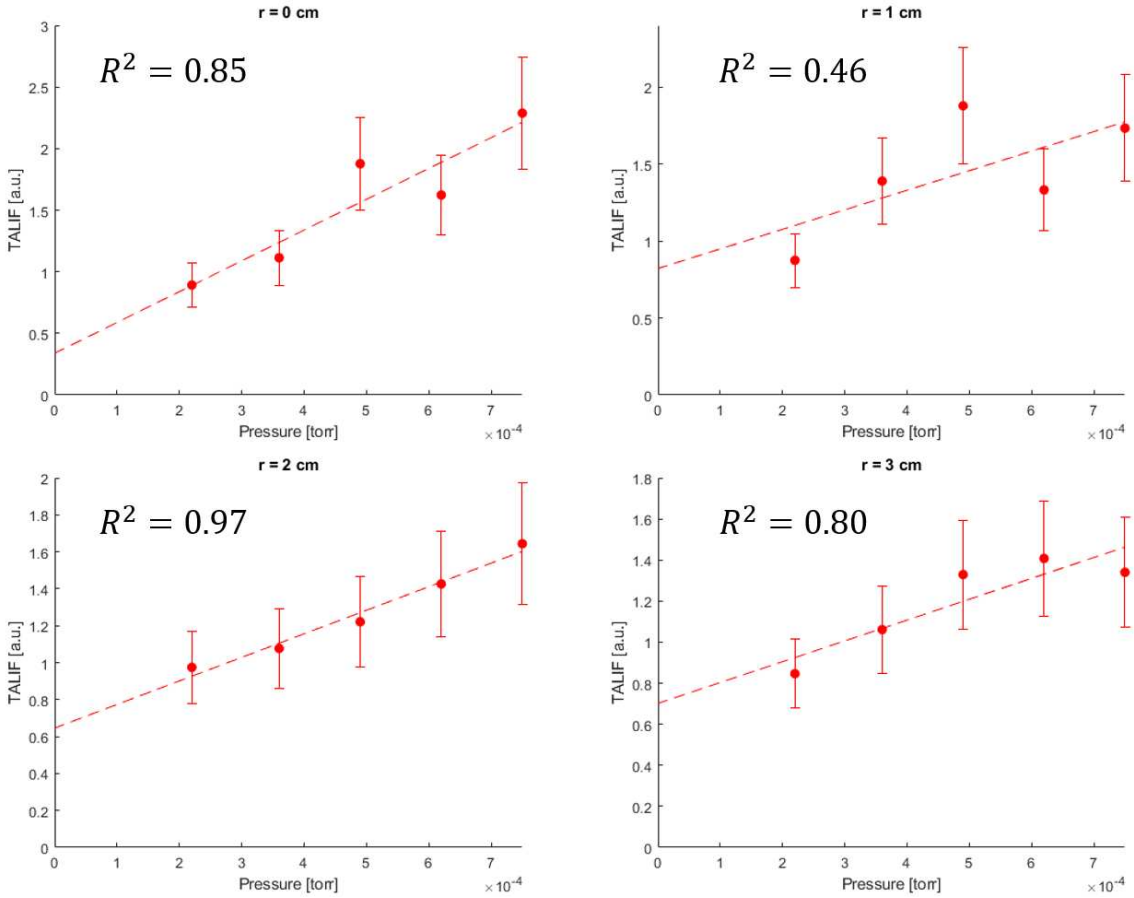

Figure 20: TALIF vs. chamber pressure at various radial positions (r).

4.4.3 Variation of Radial Measurement Position

Here, we report studies of moving the exact measurement location relative to the cathode - in the radial direction - with the BaO hollow cathode operating at fixed current of 8 A. The TALIF diagnostic technique under development is intended to be used to measure the spatial

density profile of neutral xenon in an EP plasma. Performing a radial profile measurement validates this capability in addition to providing information on the ionization characteristics at different points within the plasma.

To keep optical collection efficiency consistent between measurements, the cathode was moved along the beam path within the chamber (as this is more convenient than moving the position of the beam focus and collection optics). The dimensions of the vacuum chamber restricted this movement to within 3 cm of the center position, so data was recorded at 0-3 cm from the centerline in 1 cm steps (all 1-cm axially downstream (vertical to the beam path) of the exit plane). Again, the PMT remained fixed at 500 V gain setting. To perform the measurements, the cathode mount was translated along a rail fixed to the chamber base. Again, the laser beam was set to its peak wavelength of 222.506 nm and 100 signal averages were used. Figure 21 shows the results of the radial measurements for several different flow-rates labeled as $\dot{m}$ in each panel. Data was recorded for conditions of both plasma On and Off. In both cases, we see that in general for a given flow rate, there are lower signals (a possible local minimum) at the r = 0 cm position than at the r = 1 cm position. Intuitively, we may expect the density on the centerline (particularly in the plasma Off case) to be highest, because the gas density should immediately fall off as it diffuses into the chamber. However, signal strength increases at r = 1 cm, and begins to decrease for r >= 2 cm. The increase at r = 1 cm may be attributed to a high-pressure region near the inner wall of the cylindrical anode, while the drop at larger radial positions is due to diffusion as the gas fills the volume of the chamber. The separation between the plasma On and Off signals decreases with radial position. Similar to the density drop seen in section 4.5.1, this separation is due in part to ionization and primarily to an increase in neutral temperature. Far from the exit plane of the cathode, a combination of cooling through collisions during diffusion and a lack of ionization

events due to lower electric potential decreases the difference in neutral density between the plasma On and Off cases.

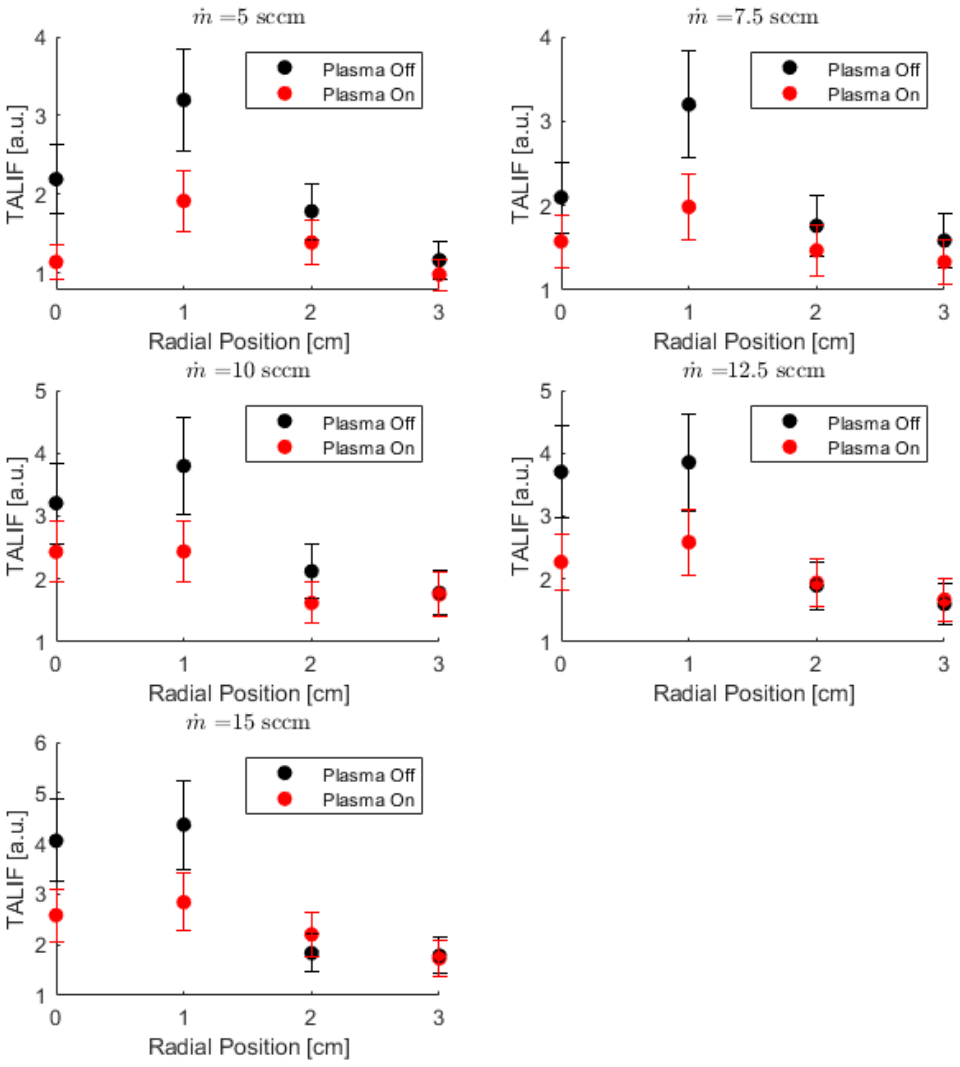

Figure 21: TALIF vs. laser focus position at various flow rates

4.4.3.1 *Study of Ionization Fraction*

As alluded to in the prior subsection, changes in TALIF signal as the plasma is turned On/Off can give insight into the spatial variation in ionization and neutral gas temperature. Examples of such data, for different radial positions and flow-rates, are shown in Figure 22. In this figure, the % difference in the TALIF signal after turning the cathode On is shown. The percent difference between two values is calculated as the difference between the two values divided by

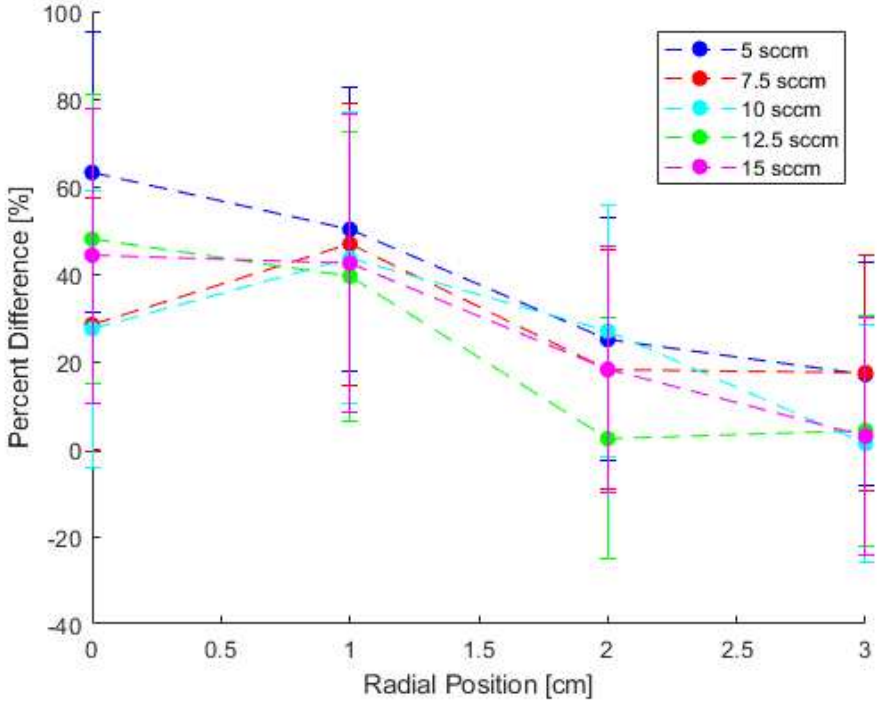

Figure 22: Percent reduction in TALIF signal as the is switched from the plasma On state to Off state. Different curves are for different flow rates

their average. The amount of error in this calculation is determined by first taking the sum and difference error (the sum of the uncertainty in each measurement) carried into a quotient error calculation (the root sum squared of the uncertainty in the numerator and denominator). The effect is strongest on the cathode centerline (r=0) where ionization and temperature are expected to be at their highest, before significant cooling and recombination through diffusion take effect.

CHAPTER 5: HALL EFFECT THRUSTER EXPERIMENTS

5.1 Introduction

All work up to this point was in support of a demonstration of TALIF measurements in the plasma plume of a Hall effect thruster. TALIF measurements in electrostatic thrusters dates back over 20 years [40], but measurement specific to HETs have been introduced within the last decade [42]. The following experiments were performed at CSU's Center for Electric Propulsion and Plasma Engineering (CEPPE) on a 1.5 kW Hall Thruster.

The thruster was mounted on the front wall of a large cylindrical vacuum chamber, which was pumped to a base pressure of 1.5×10^{-5} torr (calibrated to air) by a pair of diffusion pumps. With the move to a new lab space and a larger scale chamber, some modifications to the experimental setup were needed. Most notably, the collected light was changed to being fiber coupled out of the chamber and into the PMT. Doing so reduced the spatial resolution of the experiments from a 24 mm length along the beam (as determined by the photocathode and system magnification of 1) to a 1.8 mm length (based on fiber core of 600 μm and 3:1 magnification). The choice of fiber coupling the collection optics was made based on the lack of a clear optical path (small windows only) out of the chamber. In addition to improved spatial resolution, a fiber coupled setup is more versatile for use in different chamber configurations, should TALIF be needed as a mobile diagnostic. The entire system external to the chamber was placed on a mobile tabletop, which reduces the amount of lab space required.

5.2 Experimental Setup for Hall Effect Thruster Measurements

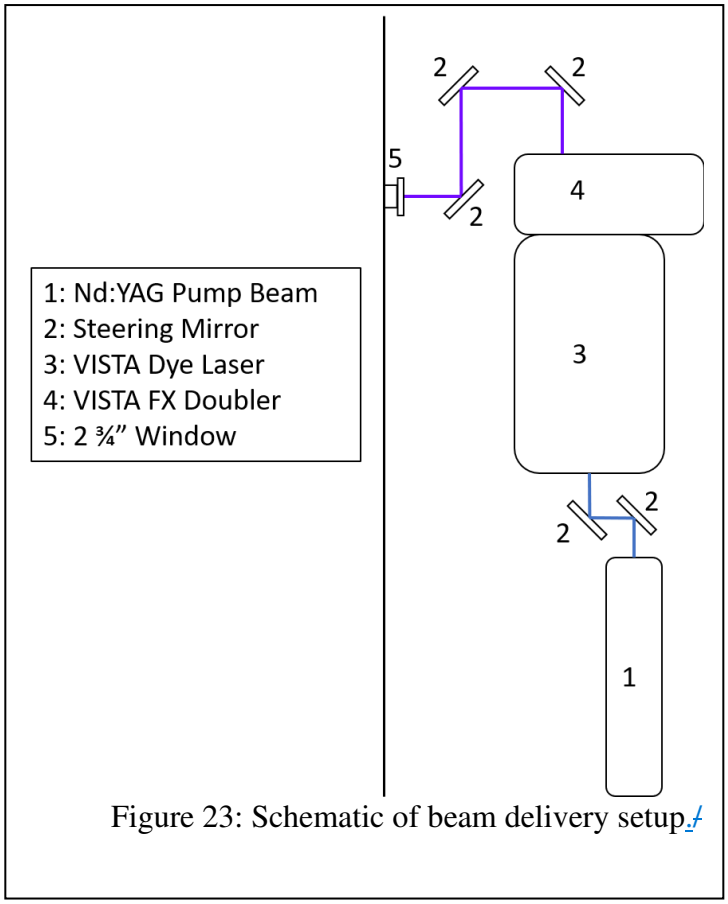

Figure 23: Schematic of beam delivery setup.

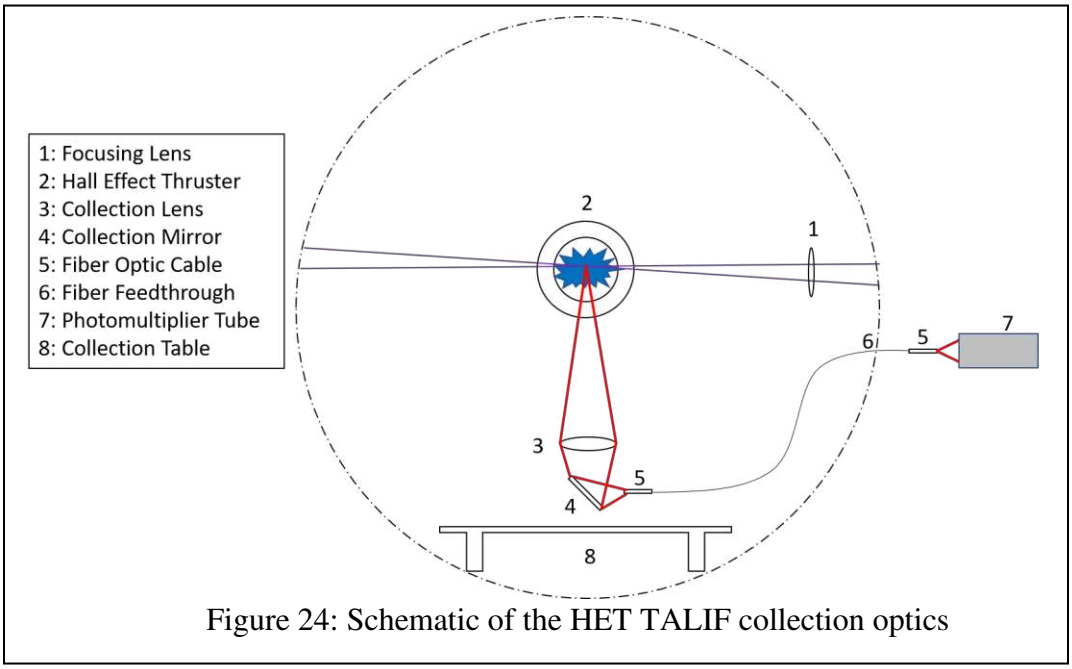

Figure 24: Schematic of the HET TALIF collection optics

The experimental setup for light delivery is shown in Figure 23 while the thruster and light collection is shown in Figure 24. The dye laser system consisted of the third harmonic (355 nm)

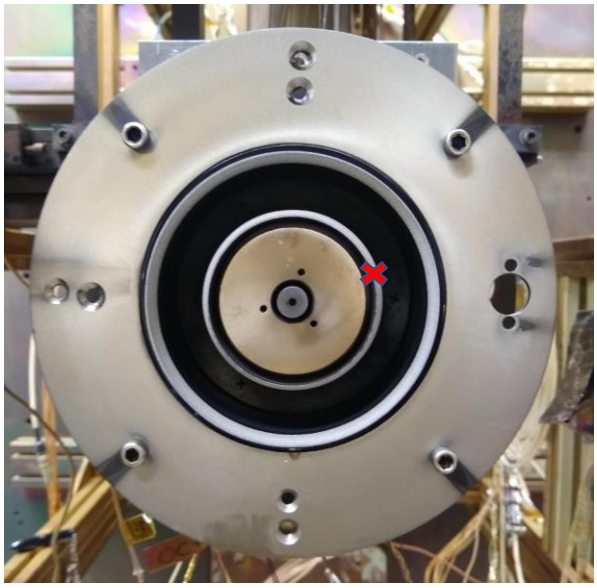

Figure 25: 1.5 kW Hall thruster with a red X marking the approximate radial position of the focus (3.3 cm from center)

of an Nd:YAG as a pump beam (Continuum Surelite III) for the actual dye laser module. The pump beam was reflected off two mirrors (Amplitude Laser 105-0160) at right angles into the dye laser (Continuum Vista) to remove the first and second harmonics. The dye (Coumarin 440) was used to generate a visible output beam at ~445 nm which was sent into the frequency doubler (Vista FX) to achieve the desired output wavelength (typically 222.506 nm). The beam was sent from the optical table exterior via steering mirrors (Lattice Optics RX-225-45-UF-1025) to the chamber through an AR coated window (ThorlabsVPCH42-UV) into the chamber. Inside the chamber, a 500 mm focusing lens (Thorlabs LA4184) brought the beam to a weak focus at the measurement location. On the opposite end of the chamber was a black carbon sheet acting as a beam dump. The collection lens (Newport KBX160AR.16) was placed 300 mm below the beam focus and the collection mirror (Thorlabs BB2-E03) reflected the collected light into the optical fiber (Thorlabs M29L02). The collection lens was positioned for 3:1 imaging (with the larger

dimension of 1.8 mm on the side of the TALIF beam and smaller dimension of 0.6 mm matched to the fiber diameter). This light was passed through a fiber feedthrough (Thorlabs VC2L6S) which was connected to an identical fiber exterior to the chamber. The output of the exterior fiber was sent directly into the PMT (Hamamatsu R3896) with a bandpass filter (Thorlabs FB790-10).

The focused beam waist was determined to be approximately 1.3 mm based on a knife-edge experiment. Therefore, the entire width of the beam focus could be imaged, while the emission along the beam path overfilled the fiber. The plasma background emission approached the PMT current threshold (1 mA) at a gain setting of 900 V (Gain = 3800), so this set point was used for each data point.

The thruster had a range of operating parameters as follows:

- Thrust: 70 – 100 mN
- Specific Impulse: 1500 – 1750 s
- Power: 1.3 – 1.8 kW
- Mass flow rate: 3.25- 5.6 mg/s

The thruster was a 1.5 kW SPT style thruster with a ceramic borosil (BN-SiO_2) channel. The channel dimensions were 104 mm O.D. with a width of 17 mm and a length of 32 mm. Four outer coils coupled with a center coil generated the magnetic field in the channel. A center-mounted heaterless hollow cathode ignites and feeds the plasma through electron emission and minimizes plume divergence (~ 20° half angle). Measurements were recorded at axial positions of 1.3 cm, 2.1 cm, 3 cm, 4.9 cm, and 7 cm downstream of the thruster face. The position nearest the thruster is limiting by clipping of the fluoresced light by the thruster before reaching the collection lens for positions closer than 1.3 cm. The farthest point was limited by the available dimensions of the thruster test stand.

The vacuum system was a 1.7 m diameter by 4.6 m long cylindrical chamber pumped by a Leybold DryVac 650 roughing pump and two Varian HS20 diffusion pumps. High purity (99.999% pure) xenon propellant was fed through anode and cathode gas inlets via stainless steel feed lines from a compressed gas bottle. Brooks 5850E mass flow controllers (± 2% accuracy) were used to control the mass flow rate. A Granville Phillips S260 ion gauge (± 25% accuracy) was used to monitor low chamber pressures.

The neutral density in a HET plasma has been shown to peak sharply near the thruster channel walls (considering the radial direction) [42], so the beam focus was aligned at a position 3.3 cm from the center of the thruster in order to be roughly coincident with the inner channel wall and to take advantage of expected elevated neutral densities (Red X marked on Figure 25). However, because recording data at a given position required a chamber pump down and venting cycle of approximately 4 hours, acquisition points in this study are restricted to axial positions at a fixed radius. Therefore, there is no means of confirming the focus was indeed positioned at a peak neutral density location (again, considering the radial direction). Multiple axial positions were favored over radial because there is a known (expected) asymptotic decay trend in density axially when the plasma is off [42]. The radial behavior is generally more complex and would require measurement at a higher number of positions to accurately map, making it more difficult to confirm that the TALIF signal behavior is physically meaningful.

5.3 Results for Hall Effect Thruster Experiments

5.3.1 Variation of Thruster Flow Rate

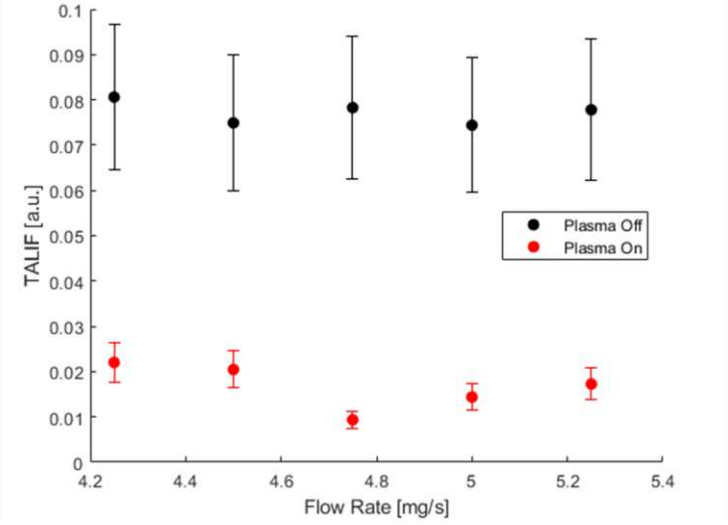

Figure 26: TALIF signal versus thruster flow rate with the plasma on and off (z = 1.3 cm)

This set of experiments was performed with the chamber first evacuated to its base pressure near 1.5 x 10^{-5} Torr. The HET discharge was turned on and set to a specified flow rate. At each measurement condition, 100 averaged signals were recorded before the thruster was turned off and the process was repeated. The critical HET parameters for these experiments included a thrust of 80 mN, specific impulse of 1600 s, and power of 1.3 kW. "Plasma On/Off" refers to "Thruster On/Off" and not any other potential plasma discharge conditions.

Results of TALIF measurements as a function of flow-rate are shown in Figure 26. To first order, when the thruster is off (or thruster is on but ionization fraction uniform), one can expect the TALIF signal to increase linearly with flow rate due to the density (chamber pressure) dependence; however, this trend is hard to see given uncertainty in the data (~20 %) versus the fairly small range of flow rates (~12% of the mean). The drop in Xe density between plasma Off to plasma On is consistent in each case at ~75%. Hall Effect thrusters have a propellant utilization efficiency typically in the range of 70-80% [58], which is consistent with the observed drop in signal. As discussed earlier, increase in gas temperature (leading to density reduction at fixed pressure) may also contribute.

To verify the recorded signals were TALIF, and to examine possible features such as spectral broadening, full absorption lines (wavelength scans) were also recorded for cases of both plasma On and Off at a position of z = 2.1 cm from the thruster face (Figure 27). The FWHM in

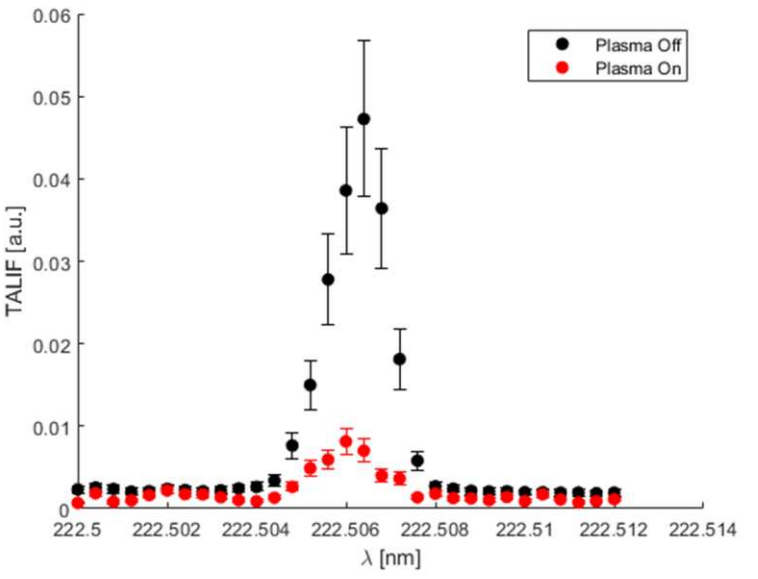

Figure 27: TALIF absorption lines in HET plume with plasma on and off (z = 2.1 cm)

each case is 0.002 nm (12.1 GHz). This value is again significantly wider than the predicted Doppler broadened calculated in section 4.5.1.1, so again it appears the broadening is being

dominated by other mechanisms, e.g., the laser as was discussed in Section 4.5.1.1. The peak signal with the plasma on is ~25% of the peak signal with the plasma off, which is consistent with the results from Figure 26.

5.3.2 Effect of Signal Averaging

Our TALIF setup used a fairly small light collection size (~1.8 mm along beam) in order to achieve desired spatial resolution for mapping of gradients and plasma structures, but at the expense of lowering signal levels. In this subsection, we investigate the effects of noise on signal collection and the possibility of using differing numbers of laser shots (with the goal of single-shot measurements at ns-time resolution). Figure 28 shows raw TALIF PMT signals recorded with 4 different numbers of laser shot accumulations (averages). For each number of accumulations, we characterize the data quality with signal-to-noise (SNR) defined as the ratio of the peak amplitude to the noise (standard deviation) in the baseline. The results show that the SNR improved from 10 shots to 100 shots (7.6 - 8.3), with larger improvement from 100 shots to 500 shots (8.3 - 10.5), and minimal change beyond 500 shots (10.5 - 10.1). The improvements in SNR with number of shots comes at a cost of acquisition time. This is of particular interest when recording absorption lines, as the laser dye energy deteriorates rapidly (~ 1 mJ drop in 15 minutes of continuous operation). To optimize this balance of SNR and acquisition time, the practice of recording 100 shot averages has been maintained.

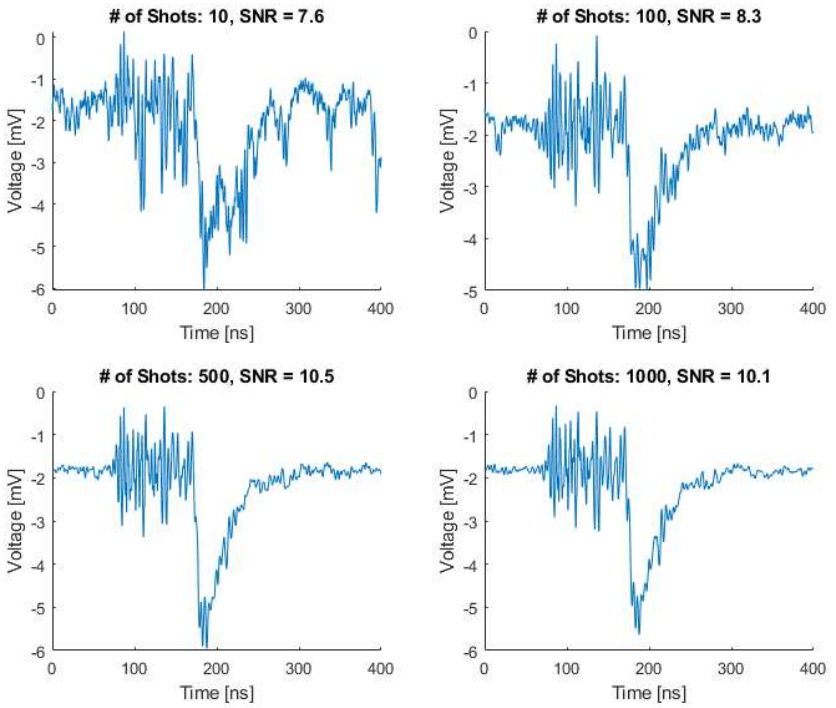

Figure 28: TALIF signals at a single operating condition recorded by averaging different numbers of laser pulses.

5.3.3 Detection Limit Estimation

In order to determine the density detection limit of neutral xenon in the HET plasma, a reference signal was obtained from a glass tube containing 4.5 x 10^{19} m^{-3} xenon. To perform this measurement, the glass tube was mounted on a tripod such that the beam passed through the length of the tube and focused at its center. The experimental setup remained the same as described in section 5.2. The peak ratio between the glass cell signal and an HET plasma signal 2.1 cm downstream at a flow rate of 4.5 mg/s in Figure 29 is 13.75. The corresponding neutral xenon density in the plasma (specific to this location in the plume) is therefore inferred to be 2.9 x 10^{18} m^{-3}. The ratio of the HET plasma signal peak to its baseline noise is 3.66, yielding an estimated detection limit of 9 x 10^{17} m^{-3}. This detection limit has proven effective for the densities encountered at the positions measured for this thruster. Additionally, this is a relatively low power

thruster, meaning it operates at lower flow rates and should have lower neutral densities within the plume. An improvement in collection efficiency would have a corresponding increase in collection of plasma background emission in addition to an increase in TALIF signal strength, so it's not clear if improving the collection of the setup will improve SNR.

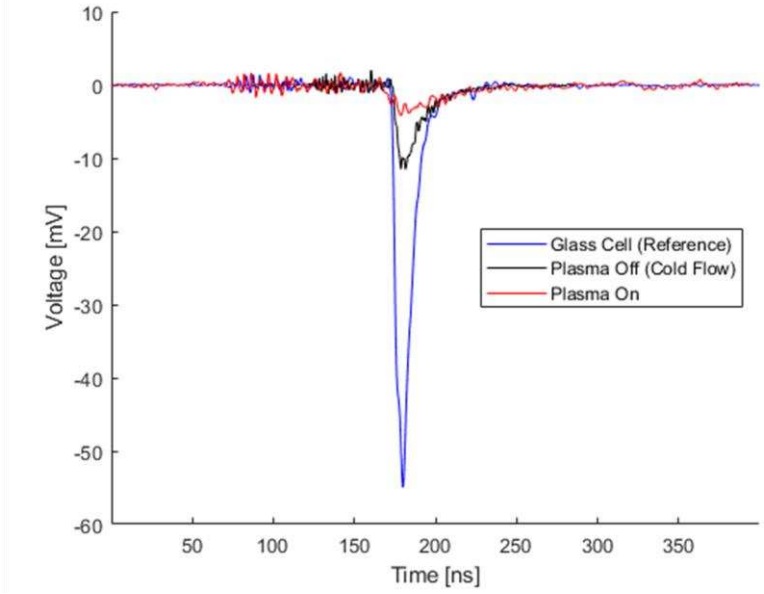

Figure 29: TALIF signal in plasma compared to a reference cell

Of note in Figure 29 is the decay time of the signal (after the peak) is longer for the plasma case than the reference signal. According to the TALIF model from chapter 2, the decay rate would be determined by the combined rates of the upper state loss mechanisms. Because the laser pulse has already passed, the only loss mechanism to control the rate of decay would be spontaneous emission. However, the spontaneous decay rate should be a fixed property of the xenon excitation level and would not vary between signals. This indicates that the quench rate (collisional de-excitation rate), which would scale with xenon density, is not negligible for the 222.506 nm line over the xenon density range measured. Figure 30 shows the glass cell signal, plasma signal (both

from Figure 29), and the corresponding plasma off signal (2.1 cm downstream at 4.5 mg/s) normalized by their peak values to show their variation in decay times.

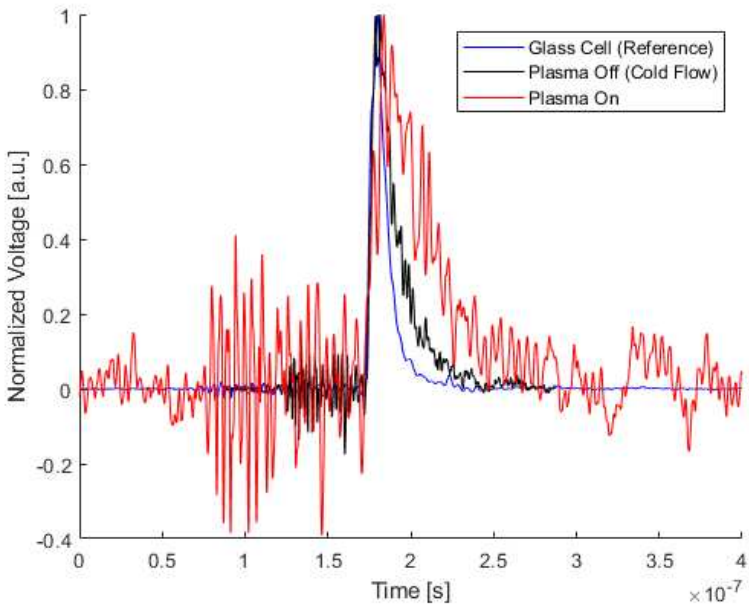

Figure 30: Comparison of the temporal profile of a TALIF signal in a reference cell, cold HET gas flow, and HET plasma

The 1/e time for the glass cell, cold flow, and plasma signals are 10.15 ns, 17.36 ns, and 31.15 ns respectively. Using the ratio of signal peak values to estimate xenon density, as done to estimate detection limit before, the respective densities are 4×10^{19} m^{-3}, 8.8×10^{18} m^{-3}, 2.9×10^{18} m^{-3}. The decay time decreases with xenon density, which matches the expected behavior of quenching [34]. Using the measured decay time from the non-plasma cases (to neglect collisional plasma dynamics), the estimated densities, and a reported spontaneous decay rate of 3.5×10^{7} s^{-1} [59], the quenching coefficients for this TALIF line would be $2.1 \pm 0.7 \times 10^{-12}$ m^3s^{-1}. Any effects quenching may have on signal peak height or area as a function of density should be accounted for with a detailed calibration curve. Acquiring such a curve will be a point of focus in the future or this project.

The detection limit of this measurement system was limited primarily by the strength of the plasma background emission signal, and how it limits the achievable gain of the PMT. This also means the detection limit varies spatially with the plasma luminous intensity. The detection limit reported here at 2.1 cm downstream of the thruster face is likely higher than it would be in the HET far field, where there is little background emission and the PMT gain can be used to scale recorded signals without damage.

5.3.4 TALIF Axial Data in HET

In this subsection, we present spatial mapping of the TALIF signal as a function of the HET axial position (at a fixed radial location). The HET mount was designed to allow for changes in axial position (while all optics were held fixed). At a given axial position of the thruster, 100 averaged shots were recorded with plasma on and then again with the plasma off. The chamber was then vented in order to move to the next position (it was not possible to change position without breaking vacuum.) The next data point was then recorded after a full pump down of the chamber and restart of the thruster. The HET operating conditions are: T = 80 mN, I_{sp} = 1600 s, and P = 1.3 kW.

Figure 31 shows the TALIF data as a function of axial position (for both HET plasma Off and On) using a flow rate of 4.5 mg/s. As can be seen in the figure, the cold-flow (plasma Off) TALIF data show an asymptotic decay which is reasonable in light of the mass discharge out of the center-mounted cathode, which is expands into the large pumped down (high Knudsen number) chamber volume. The apparent slight increase of the final axial data point at 7 cm is attributed to measurement uncertainty. The axial neutral density distribution in the plasma follows a similar decay pattern.

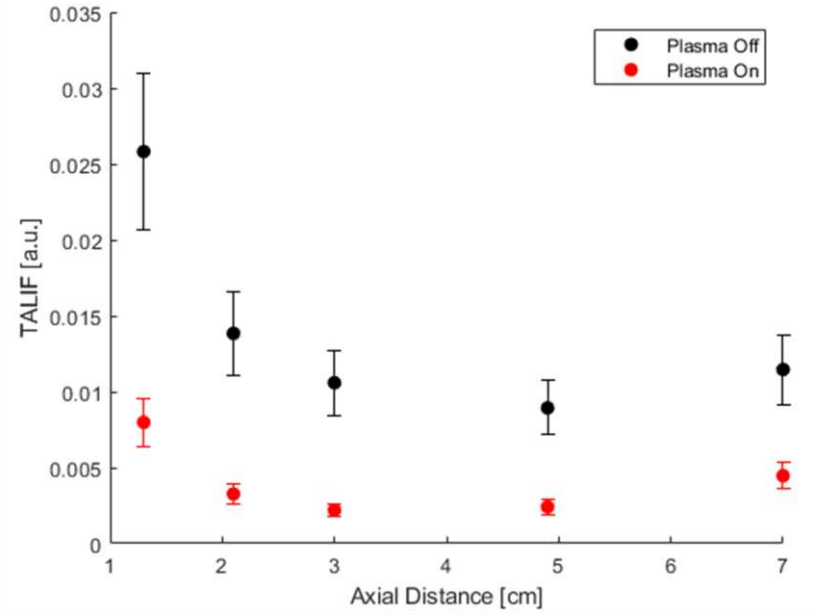

Figure 31: TALIF as a function of axial position downstream of the HET

We have also examined the signal change, at a given position, as the thruster is changed from On to Off, and associate this with ionization occurring in the channel (which causes a "loss" in the TALIF signal due to neutral xenon). Figure 32 shows the percentage reduction as a function of position, which is found to be in the range of ~65-80% at each position. These values are roughly within uncertainty of one another making it difficult to see trends. Trends, if they do exist (e.g., a

decrease in ionization fraction very near the thruster face) may be attributed to complex flow dynamics or collisional behavior as particles leave the ionization channel near the wall edges.

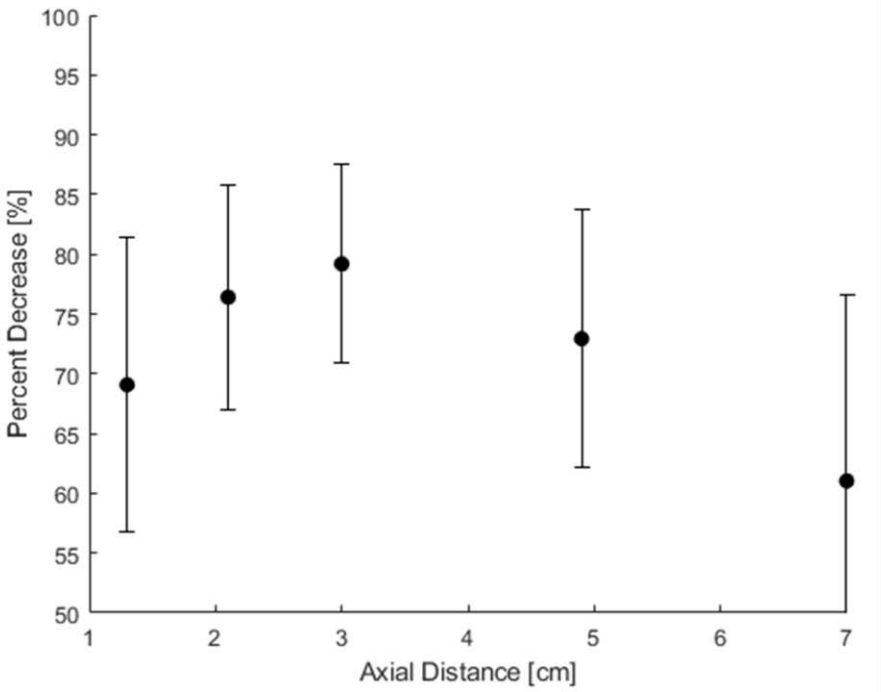

Figure 32: Percent decrease in neutral density between plasma on/off as a function of axial position downstream of the HET

CHAPTER 6: CONCLUSION

6.1 Summary

Two-photon absorption laser induced fluorescence has been demonstrated as a means to measure and analyze the density of ground state neutral xenon for electric propulsion systems. This work and others in the field seek to facilitate detailed evaluation of the impact neutral particle dynamics have on electric thruster properties like thrust, efficiency, and lifetime. This diagnostic approach acts as a means to obtain experimental data for accurate optimization and design of Hall Effect thrusters, and potentially other xenon propellant devices, for future space missions.

Chapter 2 summarized a numerical model of a cold-flow xenon TALIF signal to understand the relative contribution of particular gain and loss mechanisms. The temporal voltage profile recorded by the PMT was accurately modeled with a peak value within 6% of experimental data and a decay rate (after the laser pulse) differing by 12%. Later in the chapter, a calibration procedure used to determine xenon density in-plasma based on a known reference signal was described. The method owes its simplicity to the approximate linear relationship between xenon concentration and TALIF signal at low beam intensities.

Initial TALIF measurements in a cold-flow gas at controlled pressure was presented in Chapter 3. Spectral scans of xenon at two TALIF transitions wavelengths (249.5 and 252.5 nm) and using two available PMTs was recorded to determine the configuration yielding the highest SNR. Once the 249.5 nm transition was selected, the linear relationship between TALIF signal and xenon concentration was demonstrated, and the uncertainty in a single-shot measurement was quantified. The system detection limit was estimated as 6×10^{14} m^{-3}.

Owing to the free motion and regular collisions of electrons, a plasma has distinct optical properties from that of a gas. In chapter 4, spectral analysis of a hollow cathode xenon plasma showed the challenge plasma background emission presents to some TALIF transitions. With the move to 222.5 nm, the dependence of TALIF signal on anode current, chamber pressure, and radial position was studied. The two former showing expected behavior. Radial position studies revealed the TALIF diagnostic's ability to map spatial variation in concentration as well as thermal and ionization effects.

The work of Chapters 2-4 culminated in demonstration of TALIF measurements on a 1.5 kW Hall effect thruster. In the thruster plume, neutral xenon concentration was shown to decrease between 60-80% in the measured regions, likely due to a combination of increased neutral gas temperature in the plasma and the high propellant utilization efficiency of Hall thrusters. The detection limit of the system 2.1 cm from the thruster face was estimated to be $n_{Xe} = 9 \times 10^{17}$ m^{-3}, which is sufficient for close proximity TALIF measurements, but remains above the detection capabilities of similar works [42]. The detection limit of the system depends on the strength of the background emission by the plasma, as the DC signal can throttle the achievable gain in the PMT. Detection limit will then vary spatially with plasma emission. We may anticipate a lower detection limit in the thruster far-field. A PMT with a higher damage threshold may also permit the use of higher gain. The detection limit of 5×10^{15} m^{-3} in a Hall thruster plasma environment was deemed not feasible. That density was shown to be achievable in a cold gas environment where there is no background emission, but these results, accompanied by previous work [42] has not achieved signals lower than the order of 10^{17} m^{-3} in a plasma environment. However, the data presented here is currently the only demonstrations of TALIF on an EP thruster with a spatial resolution < 2 mm (3.14 mm^2 area). Similar work by Crofton et al. showed TALIF measurements using the 222.5 nm

line for xenon densities as low as 5 x 10^{17} m^{-3} with a spatial resolution of 5 mm^2 [42]. Fiber coupled collection optics also permit a level of versatility that allows this system to be easily integrated into measurement of various EP devices with the need for only an entrance window and a single fiber adapter port on any given vacuum chamber.

6.2 Future Work

There are three primary areas of interest for the future of this TALIF diagnostic method. Probing of regions with lower background emission may demonstrate lower density measurements, analysis of the TALIF linewidth may lead to temperature and velocimetry measurements, and the testing of krypton TALIF lines to perform thruster analysis using the alternative propellant gas

The available measurements positions, primarily axially downstream of the thruster, was limited by the range of motion of the thruster mount and the number of laser beam entrance window ports on the chamber. The expansion of measurements into this downstream region, while also possibly used for analysis of far-field propellent dynamics, can set an absolute limit on the detection limit of the system. In the far-field, the plasma would be nearly, or entirely, extinguished, meaning there should be little to no background emission limiting the PMT gain. Measuring an absolute limit can establish a reference point from which to predict the capability of the system to measure different experimental environments (i.e., high/lower power thrusters).

As explained in section 4.5.1, the linewidth of the TALIF signal did not vary with increased temperature, indicating that a line broadening mechanism other than doppler/temperature broadening is dominating the TALIF linewidth. The specified linewidth of the laser is lower than the predicted linewidth due to temperature broadening, so more needs to be done to investigate why doppler broadening has not been observed. One means to do so is to very precisely control

and test the dye concentration being fed into the laser, possibly also monitoring it as it ages. Variations in dye concentration from the optimal value can result in increased laser line broadening.

Krypton is a popular alternative to xenon as an EP propellent gas, primarily due to the reduced cost. Krypton benefits from similar characteristics to xenon, being a neutral gas with slightly lower mass (83.8 u) and higher ionization threshold (~ 14 eV), it demonstrates reduced performance that is compensated by the low cost of acquisition and production. A TALIF line with an excitation wavelength of 212 nm can be excited using the same dye laser (with a change of dye) and the fluorescence wavelength of 758.7 can be collected using the same optics (with a change of filter) [60]. As the EP industry weighs the costs and benefits of krypton propellent, the TALIF diagnostic described in this paper should be able to adapt with relative ease.

BIBLIOGRAPHY

[1] R. G. Jahn, *Physics of Electric Propulsion*. Mineola, New York: Dover Publications, 1968.

[2] "NASA Technology Roadmaps TA 2: In-Space Propulsion Technologies." pp. 2–20, 2015.

[3] J. S. Miller, S. H. Pullins, D. J. Levandier, Y. H. Chiu, and R. A. Dressler, "Xenon charge exchange cross sections for electrostatic thruster models," *J. Appl. Phys.*, vol. 91, no. 3, pp. 984–991, 2002, doi: 10.1063/1.1426246.

[4] R. R. Hofer *et al.*, "Development Status of the 12.5 kW Hall Effect Rocket with Magnetic Shielding (HERMeS)," *35th Int. Electr. Propuls. Conf.*, pp. 1–23, 2017, doi: IEPC-2017-231.

[5] M. Randolph, T., Kim, V., Kaufman, H., Kozubsky, K., Zhurin, V., Day, "Facility Effects on Stationary Plasma Thruster Testing," *27th Int. Electr. Propuls. Conf.*, pp. 844–854, 1993.

[6] I. D. Boyd, D. B. Van Gilder, and X. Liu, "Monte Carlo simulation of neutral xenon flows in electric propulsion devices," *J. Propuls. Power*, vol. 14, no. 6, pp. 1009–1015, 1998, doi: 10.2514/2.5366.

[7] H. Kamhawi, W. Huang, T. Haag, and R. Spektor, "Investigation of the effects of facility background pressure on the performance and voltage-current characteristics of the high voltage hall accelerator," *50th AIAA/ASME/SAE/ASEE Jt. Propuls. Conf. 2014*, pp. 1–17, 2014, doi: 10.2514/6.2014-3707.

[8] H. Tahara, K. Imanaka, and S. Yuge, "Effects of channel wall material on thrust performance and plasma characteristics of Hall-effect thrusters," *Vacuum*, vol. 80, no. 11–12, pp. 1216–1222, 2006, doi: 10.1016/j.vacuum.2006.01.049.

[9] F. E. Chen, *PLASMA PHYSICS AND CONTROLLED FUSION SECOND EDITION Volume 1: Plasma Physics*. 1984.

[10] J. Ashkenazy, G. Appelbaum, T. Ram-Cohen, A. Warshavsky, I. Tidhar, and L. Rabinovich, "VENμS technological payload the Israeli Hall effect thruster electric propulsion system," *47th Isr. Annu. Conf. Aerosp. Sci. 2007*, no. August, 2007, doi: 10.13140/2.1.4172.4801.

[11] W. Huang, A. D. Gallimore, and A. F. Thurnau, "Laser-induced Fluorescence Study of Neutral Xenon Flow Evolution inside a 6-kW Hall Thruster," *Laser-induced Fluoresc. Study Neutral Xenon Flow Evol. Insid. a 6-kW Hall Thruster*, pp. 1–16, 2009.

[12] K. Betz, Gerhard, Wien, "Energy and angular distributions of sputtered particles," *Int. J. Mass Spectrom. Ion Process.*, vol. 140, no. 1, 1994.

[13] E. Sommier, M. K. Scharfe, N. Gascon, M. A. Cappelli, and E. Fernandez, "Simulating plasma-induced hall thruster wall erosion with a two-dimensional hybrid model," *IEEE Trans. Plasma Sci.*, vol. 35, no. 5 I, pp. 1379–1387, 2007, doi: 10.1109/TPS.2007.905943.

[14] B. C. Lee, W. Huang, L. Tao, N. Yamamoto, A. D. Gallimore, and A. P. Yalin, "A cavity ring-down spectroscopy sensor for real-time Hall thruster erosion measurements," *Rev. Sci. Instrum.*, vol. 85, no. 5, 2014, doi: 10.1063/1.4879135.

[15] A. Shashkob, A. Lovtsov, and D. Tomilin, "Investigation into the Ionization and Acceleration regions shift in a Hall thruster channel," *Eur. Phys. J.*, 2019.

[16] NASA, "Why Do We Really Need Pressure Suits," *Aeronaut. Res. Mission Dir.*

[17] D. M. Goebel, B. A. Jorns, R. R. Hofer, I. G. Mikellides, and I. Katz, "Pole-piece Interactions with the Plasma in a Magnetically Shielded Hall Thruster," *AIAA 2014-3899*, 2014.

[18] D. N. Ruzic, *Electric Probes for Low Temperature Plasmas*. New York, New York: The American Vacuum Society Education Committee, 1994.

[19] D. Qerimi, I. Shchelkanov, G. Panici, A. Jain, J. Wegner, and D. N. Ruzic, "Radical Probe

System for In-Situ Measurements of Radical Densities of Hydrogen, Oxygen, and Nitrogen," *J. Vac. Sci. Technol.*, 2021.

[20] E. B. Saloman, "Energy Levels and Observed Spectral Lines of Xenon, Xe I through Xe LIV," *J. Phys. Chem. Ref. Data*, pp. 765–921, 2004, doi: 10.1063/1.1649348.

[21] A. Maity *et al.*, "Residual gas analyzer mass spectrometry for human breath analysis: A new tool for the non-invasive diagnosis of Helicobacter pylori infection," *J. Breath Res.*, vol. 8, no. 1, 2014, doi: 10.1088/1752-7155/8/1/016005.

[22] A. Eckbreth, *Laser Diagnostics for Combustion Temperature and Species Measurements*. Washington, D.C., 1988.

[23] J. L. Kinsey, "LASER-INDUCED FLUORESCENCE," *Ann. Rev. Phys. Chem*, vol. 28, pp. 349–372, 1977.

[24] M. J. Goeckner, J. Goree, and T. E. Sheridan, "Saturation Broadening of Laser-Induced Fluorescence from Plasma Ions," vol. 64, no. April, pp. 996–1000, 1993.

[25] T. B. Smith, "Deconvolution of Ion Velocity Distributions from Laser-Induced Fluorescence Spectra of Xenon," *Ph.D. Diss. Dept. Aerosp. Eng. Univ. Michigan*, 2003.

[26] T. Smith, B. Ngom, J. Linnell, and A. Gallimore, "Diode Laser-Induced Fluorescence of Xenon Ion Velocity Distributions," no. July, pp. 11–13, 2012, doi: 10.2514/6.2005-4406.

[27] M. Goeppert-Mayer, "Ueber Elementarakte mit Zwei Quantensprüngen," *Ann. Phys.*, vol. 114, pp. 273–294, 1931, doi: 10.1002/andp.19314010303.

[28] W. Kaiser and C. G. Garrett, "Two-Photon Excitation in CaF2: Eu2+," *Phys. Rev. Lett.*, vol. 7, no. 6, pp. 229–231, 1961, doi: 10.1103/PhysRevLett.7.229.

[29] H. Mahr, "Two-Photon Absorption Spectroscopy," in *Quantum Electronics*, H. Rabin and C. L. Tang, Eds. 1975, pp. 286–356.

[30] G. S. He, *Multi-Photon Excitation Based Nonlinear Optical Effects and Applications*, 1st ed. Elsevier B.V., 2019.

[31] A. M. Bonch-Bruevich and V. A. Khodovo, "Multiphoton Processes," *Sov. Phys. Usp.*, 1965.

[32] C. Eichhorn, S. Lohle, S. Fasoulas, H. Leiter, and M. Auweter-Kurtz, "Laser Induced Fluorescence Spectroscopy on Neutral Xenon: Two-Photon Cross Sections and Measurements in an Ion Thruster Plume," *AIAA Plasmadynamics Lasers Conf.*, 2011.

[33] H. Horiguchi, R. S. F. Chang, and D. W. Setser, " Radiative lifetimes and two-body collisional deactivation rate constants in Ar for Xe(5 p 5 6 p),Xe(5 p 5 6 p), and Xe(5 p 5 7 p) states ," *J. Chem. Phys.*, vol. 75, no. 3, pp. 1207–1218, 2003, doi: 10.1063/1.442169.

[34] C. Eichhorn, M. Winter, M. Auweter-Kurtz, and S. Lohle, "Multi-Photon Spectroscopy on Xenon for Application on Ion Thruster Plasma Parameter Investigations: Experiment and Theory," *IEPC-2007-169*, 2007.

[35] S. Kröll and W. K. Bischel, "Two-photon absorption and photoionization cross-section measurements in the $5p^5 6p$ configuration of xenon," *Phys. Rev. A*, vol. 41, no. 3, pp. 1340–1349, 1990, doi: 10.1103/PhysRevA.41.1340.

[36] S. Mazouffre, "Laser-induced fluorescence spectroscopy applied to electric thrusters," *VKI Lect. Ser.*, pp. 1–26, 2016.

[37] D. Krivoruchko, A. Skrylev, and E. Skorochod, "Multilevel kinetic model for Laser Induced Fluorescence diagnostic of a thruster with closed electron drift," no. July, pp. 1–11, 2017, doi: 10.2514/6.2017-4971.

[38] D. J. Bamford, L. E. Jusinski, and W. K. Bischel, "Absolute two-photon absorption and three-photon ionization cross sections for atomic oxygen," *Phys. Rev. A*, vol. 34, no. 1, pp.

185–198, 1986, doi: 10.1103/PhysRevA.34.185.

[39] C. G. and L. C. B. Michael B. Rankin, Jon P. Davis, “Rankin_1988.pdf.” 1988.

[40] M. Crofton, “Measurement of neutral xenon density profile in an ion thruster plume,” *AIAA Plasmadynamics Lasers Conf.*, 1996, doi: 10.2514/6.1996-2290.

[41] K. Kinefuchi, Y. Nunome, S. Cho, R. Tsukizaki, and T. L. Chng, “Two-photon absorption laser induced fluorescence with various laser intensities for density measurement of ground state neutral xenon,” *Acta Astronaut.*, vol. 161, no. January, pp. 382–388, 2019, doi: 10.1016/j.actaastro.2019.03.018.

[42] M. W. Crofton *et al.*, “Neutral Xenon Density in the SPT-140 Near-Field Plume,” *33rd Int. Electr. Propuls. Conf.*, no. IEPC Paper 2013-399, pp. 1–41, 2013.

[43] K.~Niemi, V. ~Schultz-vo. der Gathen, and H.~F.~Döbele, “Absolution Calibration of Atomic Density Measurements by Laser-Induced Fluorescence Spectroscopy with Two-Photon Excitation,” *J. Phys. D*, vol. 34, pp. 2330–2335, 2001.

[44] D. J. Bamford, A. P. Hickman, M. J. Dyer, and W. K. Bischel, “Comparative photon statistics of several ultraviolet laser systems determined by transient two-photon absorption,” *J. Opt. Soc. Am. B*, vol. 5, no. 7, p. 1369, 2008, doi: 10.1364/josab.5.001369.

[45] W. J. Alford, “State-to-state rate constants for quenching of xenon 6p levels by rare gases,” *J. Chem. Phys.*, vol. 96, no. 6, pp. 4330–4340, 1992, doi: 10.1063/1.462862.

[46] R. J. Cedolin, W. A. Hargus, P. V. Storm, R. K. Hanson, and M. A. Cappelli, “Laser-induced fluorescence study of a xenon Hall thruster,” *Appl. Phys. B Lasers Opt.*, vol. 65, no. 4–5, pp. 459–469, 1997, doi: 10.1007/s003400050297.

[47] H. Griem, *Principles of Plasma Spectroscopy*. Cambridge: Cambridge University Press., 1997.

[48] C. Eichhorn, M. Winter, M. Auweter-Kurtz, and S. Löhle, “Theoretical and Experimental Approach of Multi-Photon Spectroscopy on Xenon for Application on Ion Thruster Plasma Parameter Investigation,” pp. 1–11, 2012, doi: 10.2514/6.2007-3878.

[49] A. Aanesland, L. Liard, G. Leray, J. Jolly, and P. Chabert, “Direct measurements of neutral density depletion by two-photon absorption laser-induced fluorescence spectroscopy,” *Appl. Phys. Lett.*, vol. 91, no. 12, 2007, doi: 10.1063/1.2786601.

[50] C. J. Wordingham, P. C. R. Taunay, and E. Y. Choueiri, “A Critical Review of Orificed Hollow Cathode Modeling : 0-D Models,” pp. 1–52.

[51] A. N. Grubisic and S. B. Gabriel, “Thrust Production Mechanisms in Hollow Cathode Microthrusters,” pp. 1–18, 2010.

[52] I. G. Mikellides, “Numerical Simulations of a Hall Thruster Hollow Cathode Plasma,” pp. 1–12, 2007.

[53] A. Friss, “Submitted by,” 2019.

[54] D. Griffiths, *Introduction to Electrodynamics*, 4th ed. Cambridge: Cambridge University Press., 2017.

[55] P. W. Milonni and J. H. Eberly, *Lasers*, Illustrate. Wiley, 1988.

[56] W. Nagourney, *Quantum Electronics for Atomic Physics and Telecommunications*, 2nd ed. Seattle, Washington: Oxford University Press, 2014.

[57] M. D. Plimmer, “Isotope shift in xenon by Doppler-free two-photon laser spectroscopy spectroscopy,” 1989.

[58] A. D. Gallimore and A. F. Thurnau, “The Physics of Spacecraft Hall-Effect Thrusters.” Plasmadynamics and Electric Propulsion Laboratory, 2008.

[59] W. F. Meggers and C. J. Humphreys, “Interference Measurements in the Spectra of Noble

Gases," *J. Res. Natl. Bur. Stand. (1934).*, vol. 13, 1934.

[60] C. Eichhorn, F. Scholze, C. Bundesmann, D. Spemann, H. Neumann, and H. Leiter, "Two-Photon Laser-Induced Fluorescence in a Radiofrequency Ion Thruster Plume in Krypton," *J. Propuls. Power*, vol. 35, no. 6, pp. 1175–1178, 2019, doi: 10.2514/1.b37487.

APPENDIX A: PHASE 1 RESULTS

Prior to the completion of the work outlined in this thesis, our group performed preliminary experiments validating TALIF as a means to measure xenon densities at the required concentration of 10^{15} m^{-3}. The experiments were similar to that described in Chapter 3, focusing on detection limit and signal noise.

A.1 Experimental Setup

The experimental setup used for TALIF experiments is shown schematically in Figure 33. The third harmonic of an Nd:YAG laser (Continuum Powerlite 8010) at λ = 355 nm was used to pump an optical parametric oscillator (Sunlite EX). The OPO allows one to access a broad range of wavelengths $\lambda = 445 - 1750$ nm with an output power of E ~ 30 mJ. The output from the OPO was subsequently passed through a frequency doubler (Continuum FX-1) in order to reach the UV wavelengths required for TALIF. The choice of the 252 nm transition was motivated by the high branching ratio (see Table 2) along with a better PMT quantum efficiency at 823 nm compared to 828 nm. The laser output from the frequency doubler was steered with a pair of dielectric mirrors and focused using a plano-convex lens (f=500 mm) inside of a vacuum cell. The TALIF signal was collected perpendicular to the optical axis using a plano-convex lens (f=40 mm) and imaged 1-to-1 onto the detection array of a PMT (Hamamatsu R3896). Additionally, the shot-to-shot laser energy was monitored using a photodiode (DET-10A). The PMT signal was collected using an oscilloscope (Tektronix TDS5034B) and the results are post-processed using MATLAB.

The vacuum chamber used (Figure 33) was filled with a mixture of He and Xe (containing 10 ppm of Xe) and the xenon number density was set by varying the chamber pressure. For pressures lower than 1 mbar (corresponding to $n_{Xe} = 2.7 \times 10^{17}\ m^{-3}$), the chamber was converted

into a flow system using a mass flowmeter (Unit Instruments 7360) and the concentration of xenon was established inside the chamber by varying the gas mixture flowrate.

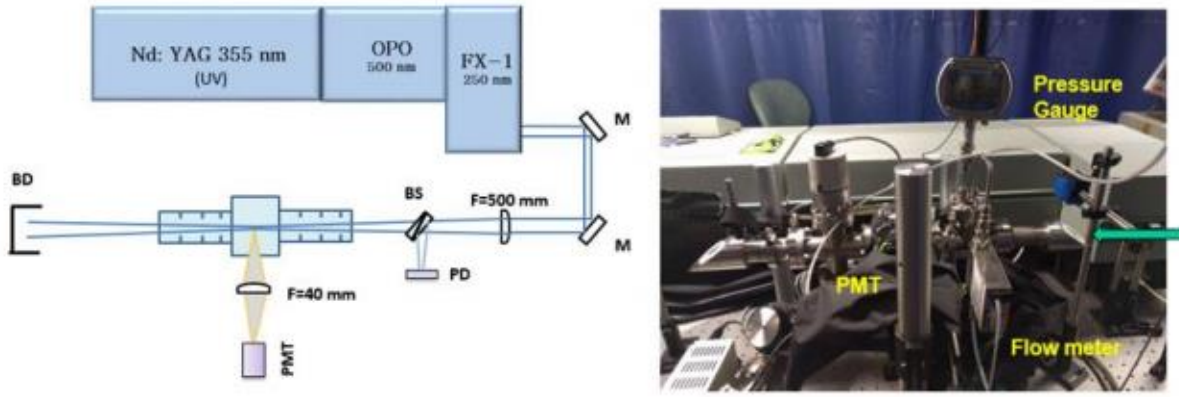

Figure 33: Optical layout used for TALIF experiments (left) and an image showing the vacuum chamber and fluorescence collection setup (right)

A.2 Results

A.2.1 Spectra

Figure 34 shows TALIF excitation spectra recorded as a function of laser wavelength for several xenon densities. These measurements were accumulated from 256 laser shots at each wavelength. The TALIF signal measurement at $n_{Xe} = 2.7 \times 10^{14}$ m^{-3} establishes a detection limit

lower than that demonstrated in recent ion thruster TALIF experiments [34], [40]. If this detection limit can be maintained, it is very adequate for expected Hall thruster conditions.

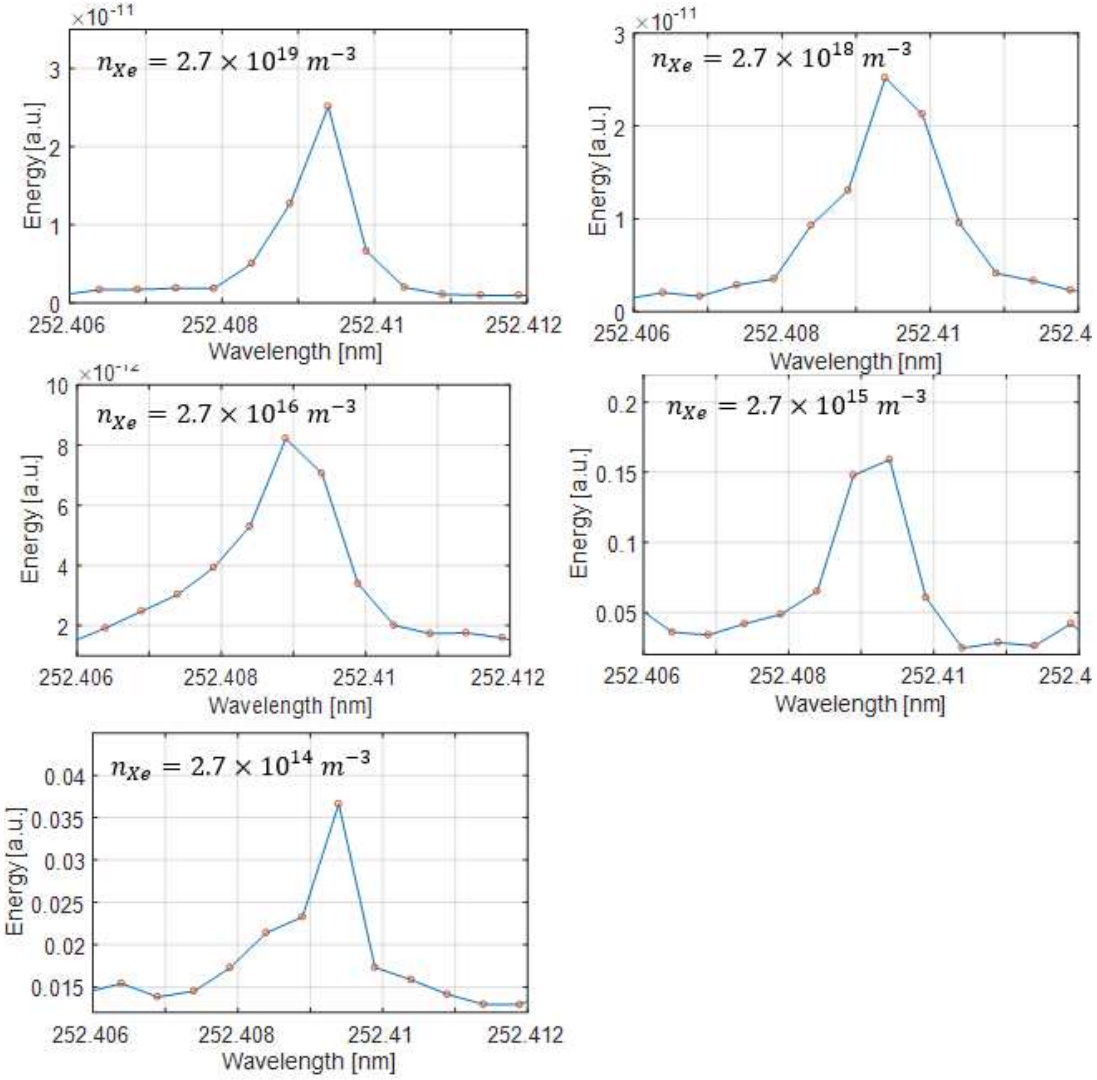

Figure 34: TALIF excitation scans at varying xenon densities. The horizontal axis was recorded directly from the OPO. More recent trials using a wavelength meter (High Finesse WS5) recorded the peak at λ = 252.415 ± .003 nm.

A.2.2 Noise Limitation and Single-Shot Detection

This study also explored the ability to make single-shot laser measurements, which is preferred over accumulating multiple shots as it corresponds to a time resolution of 10 ns (i.e., the length of exciting laser pulse). Relatively high signal-to-noise single-shot TALIF was

demonstrated at 2.7 x 10^{17} m^{-3} xenon density with a ±20% uncertainty. Statistical analysis of the data shown in Figure 35 also shows comparable (fractional) standard deviation with and without power normalization which implies the variation in laser energy is not causing the variations in TALIF signal strength. Instead, it is likely that the 2+1 photoionization loss mechanism is varying with the beam intensity profile. This variation is a stochastic process, matching the observed variation in TALIF signal. These measurements support the ability to measure with high temporal resolution (~10 ns) and spatial resolution (~5 mm in this case) at low xenon densities.

An estimate of the signal-to-noise ratio (S/N) for a single-shot measurement at the desired minimum concentration can be made as follows. The data of Figure 35 show that the noise-to-signal ratio at a concentration of 2.7 × 10^{17} m^{-3} is 0.2, corresponding to a SNR of 5. In the shot noise limit, the SNR will scale as the square root of the number of photons. At a concentration of 5 × 10^{15} m^{-3}, the number of xenon atoms, and thus the number of fluorescence photons, is about 50 times less, so the SNR should be about one seventh of what it is at 2.7 × 10^{17} m^{-3}. Thus, the SNR at 5 × 10^{15} m^{-3} approaches unity, and this represents the lower limit of detection for a single

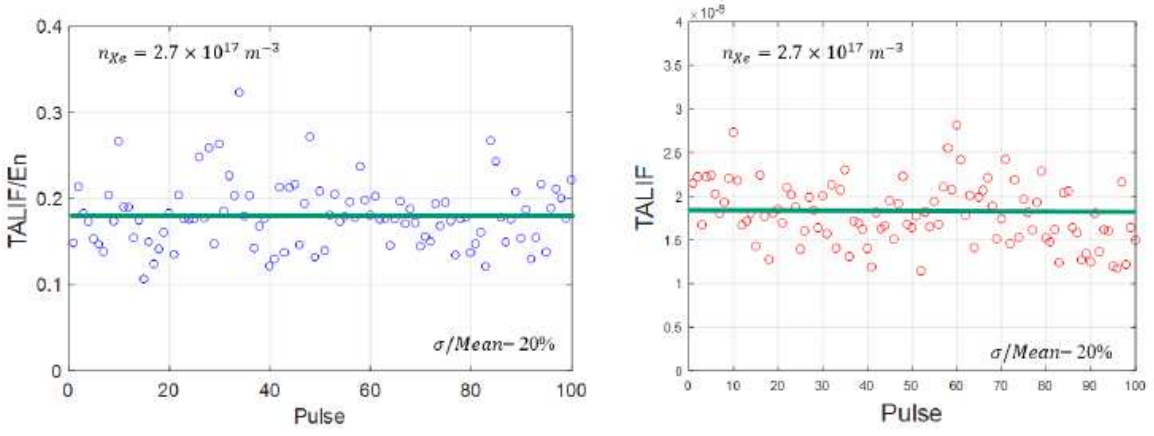

Figure 35: (left): Scattered plot of normalized (by pulse energy) TALIF signal for a number density of 2.7 x 10^{17} m^{-3}. (right): Similar plot for the raw TALIF signal. The green line represents the average TALIF over 100 laser shots

shot.

APPENDIX B: TALIF VS. BEAM ENERGY MODEL

To support the approximation that TALIF signal is varying linearly with incident beam energy, the model described in chapter 2 is used to verify that a linear approximation is valid at low energies. In Figure 36, modeled voltage is plotted against incident beam energy at a fixed xenon density.

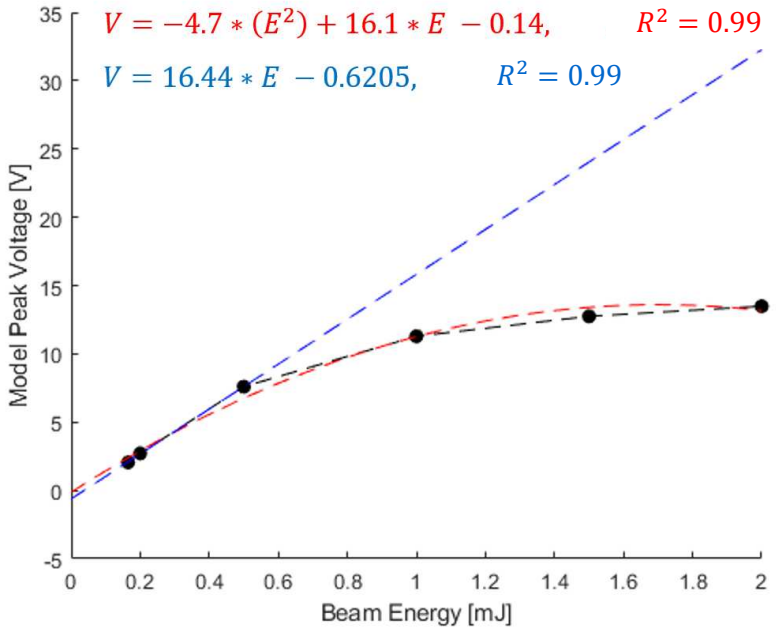

Figure 36: Xenon TALIF model results for signal dependence on beam energy

The model predicts a highly linear trend for low beam energies, before diverging toward quadratic behavior. Though the full range over which this linearity holds is not accurately captured by the model (linearity is confirmed up to 3 mJ in section 4.4), the trend extracted from the rate equation model validates the observed behavior in section 4.4. The energy range of the model and the reported results in chapter 4 cannot be directly compared because the model is written using known spectroscopic parameters for the 252.5 nm line used in chapter 3.